AD-A230 428

FILE COPY

DTIC
ELECTE
JAN 08 1991
D
D

FRACTAL GEOMETRY SEGMENTATION OF HIGH RESOLUTION POLARIMETRIC SYNTHETIC APERTURE RADAR DATA

THESIS

Joseph Lee Brickey
Captain, USAF

AFIT/GE/ENG/90D-06

DISTRIBUTION STATEMENT A
Approved for public release;
Distribution Unlimited

DEPARTMENT OF THE AIR FORCE
AIR UNIVERSITY
AIR FORCE INSTITUTE OF TECHNOLOGY

Wright-Patterson Air Force Base, Ohio

91 1 3 139

AFIT/GE/ENG/90D-06

DTIC
ELECTE
JAN 08 1991
S D
D

FRACTAL GEOMETRY SEGMENTATION OF HIGH RESOLUTION POLARIMETRIC SYNTHETIC APERTURE RADAR DATA

THESIS

Joseph Lee Brickey
Captain, USAF

AFIT/GE/ENG/90D-06

Approved for public release; distribution unlimited.

AFIT/GE/ENG/90D-06

FRACTAL GEOMETRY SEGMENTATION OF HIGH RESOLUTION POLARIMETRIC SYNTHETIC APERTURE RADAR DATA

THESIS

Presented to the Faculty of the School of Engineering
of the Air Force Institute of Technology
Air University
In Partial Fulfillment of the
Requirements for the Degree of
Master of Science in Electrical Engineering

Joseph Lee Brickey, B.S.E.E.
Captain, USAF

December, 1990

Accesion For
NTIS CRA&I
DTIC TAB
Unannounced
Justification
By
Distribution /
Availability Codes
Dist | Avail and/or Special
A-1

Approved for public release; distribution unlimited.

Acknowledgments

This thesis would have never been possible if not for the dedication of my sponsors Mike Bryant and Kevin Willey from the Automatic Target Recognition Technology Group, Aeronautical Systems Division Wright-Patterson AFB OH I would like to express my gratitude to Mike and Kevin for the continuous support they provided during this research effort. Not only did they provide state of the art equipment but they allowed unrestricted access to their expertise.

I would also like to express thanks to my thesis committee for the assistance they provided. My thesis advisor, Dr. David Meer, introduced me to Fractal Geometry and provided constant guidance along the way. Dr. Matt Kabrisky stimulated my desire to solve pattern recognition problems with thought-provoking lectures and discussions. Dr. Steve Rogers' contagious enthusiasm served as a driving force pushing me into new areas of exploration.

I want to thank Bruce Clay for the assistance he provided by allowing me to take advantage of his knowledge of UNIX, VMS, and DOS operating systems.

I would especially like to thank my wife Leann and my children Jill and Stephen for the love, support, and encouragement they provided. Without their support I would have never been able to finish.

Most of all, I want to thank my Lord and Savior, Jesus Christ, for providing this opportunity and giving me the ability to successfully complete this endeavor.

Joseph Lee Brickey

Table of Contents

	Page
Acknowledgments	ii
Table of Contents	iii
List of Figures	vi
List of Tables	x
Abstract	xi
I. Introduction	1
1.1 Background	1
1.2 Problem Statement	2
1.3 Summary of Current Knowledge	3
1.4 Scope	4
1.5 Assumptions	4
1.6 Approach	5
1.7 Hardware and Software Requirements	6
1.8 Sequence of Presentation	6
1.9 Summary	7
II. Fractal Geometry	8
2.1 Introduction	8
2.2 Overview	8
2.3 Fractals	8
2.4 Image Segmentation	11
2.5 Measuring Fractal Dimension	12
2.6 Summary	15

Page

III. Methodology 17

3.1 Introduction 17

3.2 Overview 17

3.3 Approach 18

3.4 Advanced Detection Technology Sensor 20

3.5 Data Sets 21

3.6 Calculation of Correlation Dimension 23

3.7 Viewing Correlation Dimension Estimates as Imagery . . . 25

3.8 Artificial Neural Networks 26

3.8.1 Kohonen Neural Network 26

3.8.2 Radial Basis Function 29

3.9 Summary 31

IV. Results 33

4.1 Overview 33

4.2 Correlation Dimension Image Generation 33

4.3 Distance Calculation Parameter 34

4.4 Window Size Determination 36

4.5 ADTS Imagery 36

4.5.1 M85F27 38

4.5.2 M85F28 39

4.5.3 M85F30 40

4.5.4 M98F07 41

4.5.5 M98F08 42

4.5.6 M98F09 43

4.5.7 M98F10 44

4.5.8 M98F11 45

4.5.9 M98F12 46

Page

4.6 Evaluation of Segmentation 47

4.7 Evaluation Methods 47

4.8 Analytical Evaluation 49

4.8.1 Tree–Field Boundary Analysis 49

4.8.2 Field-Shadow Boundary Analysis 55

4.8.3 Optimum Median Filter Selection 55

4.8.4 Imagery Resulting From Analytical Evaluations . 59

4.9 Subjective Evaluation 66

4.9.1 M85F30 Subjective Evaluation 70

4.9.2 M98F09 Subjective Evaluation 73

4.9.3 M98F10 Subjective Evaluation 77

4.10 Neural Network Results 80

4.10.1 Kohonen Neural Network 80

4.10.2 Radial Basis Function 81

4.11 Summary 90

V. Conclusion and Recommendations 91

5.1 Introduction 91

5.2 Overall Results 91

5.3 Recommendations for Future Research 92

5.4 Summary 93

Appendix A. Conversion To SUN Format 94

Appendix B. Fractal.C 95

Bibliography 102

Vita 105

List of Figures

Figure		Page
1.	Dimension Determination of Self-Similar Objects	10
2.	Fractal Dimension Estimation	13
3.	Block Diagram of Methodology	19
4.	M98F08 HH Polarization	22
5.	Aerial Photograph M98F08	22
6.	Kohonen Neural Network Architecture	28
7.	Radial Basis Function Network	30
8.	Example of a Two-dimensional RBF	31
9.	Hand Segmented Template M98F08	34
10.	Segmented M98F08 Using Magnitude Values Only	35
11.	Segmented M98F08 Using Magnitude and Phase Values	35
12.	Segmented M98F08 Using Phase Values Only	35
13.	M85F27 HH Polarization 1024×512	38
14.	Hand Segmented Template M85F27	38
15.	M85F28 HH Polarization 1024×512	39
16.	Hand Segmented Template M85F28	39
17.	M85F30 HH Polarization 1024×512	40
18.	Hand Segmented Template M85F30	40
19.	M98F07 HH Polarization 1024×512	41
20.	Hand Segmented Template M98F07	41
21.	M98F08 HH Polarization 1024×512	42
22.	Hand Segmented Template M98F08	42
23.	M98F09 HH Polarization 1024×512	43
24.	Hand Segmented Template M98F09	43

Figure Page

25. M98F10 HH Polarization 1024 × 512 44

26. Corner Reflector Template M98F10 44

27. M98F11 HH Polarization 1024 × 512 45

28. Hand Segmented Template M98F11 45

29. M98F12 HH Polarization 1024 × 512 46

30. Hand Segmented Template M98F12 46

31. Threshold Sensitivity Plot M98F11 All Polarizations WS 16 × 16 . . 48

32. M85F27 HH Polarization 60

33. Segmented M85F27 Tree-Field-Shadow WS 16 × 16 60

34. Segmented M85F27 Tree-Field-Shadow WS 8 × 8 60

35. M85F28 HH Polarization 61

36. Segmented M85F28 Tree-Field-Shadow WS 16 × 16 61

37. Segmented M85F28 Tree-Field-Shadow WS 8 × 8 61

38. M98F07 HH Polarization 62

39. Segmented M98F07 Tree-Field WS 16 × 16 62

40. Segmented M98F07 Tree-Field WS 8 × 8 62

41. M98F08 HH Polarization 63

42. Segmented M98F08 Tree-Field WS 16 × 16 63

43. Segmented M98F08 Tree-Field WS 8 × 8 63

44. M98F11 HH Polarization 64

45. Segmented M98F11 Tree-Field WS 16 × 16 64

46. Segmented M98F11 Tree-Field WS 8 × 8 64

47. M98F12 HH Polarization 65

48. Segmented M98F12 Tree-Field WS 16 × 16 65

49. Segmented M98F12 Tree-Field WS 8 × 8 65

50. Histogram of M85F30 All Polarizations 16 × 16 67

51. Histogram of M98F09 All Polarizations 16 × 16 68

Figure Page

52. Histogram of M98F10 All Polarizations 16 × 16 69

53. M85F30 HH Polarization 71

54. M85F30 Correlation Dimension Image 71

55. M85F30 Hand Segmented Template 71

56. M85F30 Corner Reflector Template 72

57. Segmented M85F30 Culture 72

58. Segmented M85F30 Culture/Trees 72

59. M98F09 HH Polarization 74

60. M98F09 Correlation Dimension Image 74

61. M98F09 Hand Segmented Template 74

62. M98F09 Hand Segmented Template 64 × 32 75

63. Segmented M98F09 Culture 75

64. Segmented M98F09 Culture Median Filtered 75

65. M98F09 Hand Segmented Template 128 × 64 76

66. Segmented M98F09 Culture 76

67. Segmented M98F09 Culture HH Polarization 76

68. M98F10 HH Polarization 78

69. M98F10 Correlation Dimension Image 78

70. M98F10 Corner Reflector Template 1024 × 512 78

71. M98F10 Corner Reflector Template 64 × 32 79

72. Segmented M98F10 Corner Reflectors 79

73. Segmented M98F10 Corner Reflectors/Grass Boundaries 79

74. M85F28 RBF Training Regions 83

75. M85F27 HH Polarization 84

76. M85F27 RBF Output (15 Features) WS 16 × 16 84

77. M85F27 RBF Output (4 Features) WS 16 × 16 84

78. M85F28 HH Polarization 85

Figure Page

79. M85F28 RBF Output (15 Features) WS 16 × 16 85

80. M85F28 RBF Output (4 Features) WS 16 × 16 85

81. M98F07 HH Polarization 86

82. M98F07 RBF Output (15 Features) WS 16 × 16 86

83. M98F07 RBF Output (4 Features) WS 16 × 16 86

84. M98F08 HH Polarization 87

85. M98F08 RBF Output (15 Features) WS 16 × 16 87

86. M98F08 RBF Output (4 Features) WS 16 × 16 87

87. M98F11 HH Polarization 88

88. M98F11 RBF Output (15 Features) WS 16 × 16 88

89. M98F11 RBF Output (4 Features) WS 16 × 16 88

90. M98F12 HH Polarization 89

91. M98F12 RBF Output (15 Features) WS 16 × 16 89

92. M98F12 RBF Output (4 Features) WS 16 × 16 89

List of Tables

Table		Page
1.	Calculation of Correlation Dimension	25
2.	Tree-Field Percentage Correct Window Size 16×16	50
3.	Tree-Field Percentage Correct Window Size 16×16 (M85F27 not included)	52
4.	Tree-Field Correlation Dimension Thresholds Window Size 16×16	53
5.	Tree-Field Percentage Correct Window Size 8×8	54
6.	Tree-Field Correlation Dimension Thresholds Window Size 8×8	56
7.	Field-Shadow Percentage Correct	57
8.	Field-Shadow Correlation Dimension Thresholds	58
9.	Comparison Between 3×3 and 5×5 Median Filter Operation	59
10.	Radial Basis Function Output Evaluation	82
11.	Conversion From VMS 8-8-4 Format to UNIX Format	94

AFIT/GE/ENG/90D-06

Abstract

This thesis investigated the potential of fractal dimension estimation for segmenting high resolution polarimetric synthetic aperture radar. The data used during this research were collected with the Advanced Detection Technology Sensor (ADTS) developed by Massachusetts Institute of Technology Lincoln Laboratory with Defense Advanced Research Projects Agency funding. ADTS is a fully polarimetric calibrated 35 GHz SAR with one foot impulse response. A method of applying the correlation dimension algorithm developed by Grassberger and Procaccia for estimating the dimension of time series data was implemented to estimate the correlation dimension of polarimetric SAR data.

A threshold sensitivity study was performed to determine which combination of polarizations used to calculate the correlation dimension resulted in the most accurately segmented image. Correlation dimension estimates were shown to be valid and robust features for segmenting ADTS imagery into culture, tree, field, and shadow regions. Simple thresholding and median filtering of correlation dimension estimates calculated from non–overlapping windows of ADTS imagery produced segmented imagery that was consistently over 90% accurate when using all four linear polarizations. An approach was implemented for automatically distinguishing between different classes of naturally occurring regions within the SAR image using correlation dimension estimates as input features to artificial neural networks.

FRACTAL GEOMETRY SEGMENTATION OF HIGH RESOLUTION POLARIMETRIC SYNTHETIC APERTURE RADAR DATA

I. Introduction

1.1 Background

Pattern recognition research at the Air Force Institute of Technology (AFIT) has been working toward the goal of building a guidance system for an autonomous missile. The capabilities of this missile will vary depending on the type of target the missile is designed to attack. If the missile is designated to attack a target at a known fixed location, the missile's inertial navigation system will deliver the weapon to the vicinity of the target. At that time a terminal guidance system will take over and direct the weapon to the approximate target location. The accuracy of the weapon will depend on the system's ability to correlate a stored target image with sensor input. However, designing a missile capable of attacking mobile targets is a much harder task. This missile must be capable of performing a wide area search, locating potential targets within the search area, then identifying and destroying the particular target of interest. For this system to be feasible, a pattern recognition system with a zero false alarm rate must be employed since the missile will strike on the first detection. If this first detection is a false alarm, the missile is wasted on a non–target. Worse yet, the false alarm could be a non–military object or an object of friendly origin. The type of sensor for this mission is an unanswered question. Different missions require different sensor types (i.e. active or passive) and different frequency ranges (i.e. visible, infrared, microwave). The sensor requirements

for finding moving tanks on a desert battlefield vary greatly from finding camouflaged vehicles at ambient temperature in a European environment. In general, the capability to locate and destroy mobile targets autonomously does not exist.

Since the goal of developing a sensor suite capable of autonomously locating and identifying targets has not been realized, intermediate steps must be taken to achieve this goal. Technological advancement in sensor design has produced airborne sensors capable of collecting far more data than can be reasonably handled by aircrews. If a pattern recognition system could be designed that would provide the capability to detect and identify targets in real–time with a man in the loop then as technology advances that capability could be implemented on an autonomous missile.

One step towards the development of a real–time detection/identification capability and the ultimate goal of an autonomous missile would be the development of a pattern recognition system capable of locating all man–made items within a sensor's field of view. This man–made object detector would allow the human eye and brain to aid in the identification process. The aircrew would only have to view imagery containing cultural items thus greatly reducing the amount of data requiring attention.

1.2 Problem Statement

This thesis research investigated the potential of fractal dimension estimation to segment high resolution polarimetric synthetic aperture radar imagery. The goal was to determine if correlation dimension estimates were capable of segmenting one foot impulse response polarimetric SAR imagery into cultural, tree, field, and shadow regions.

1.3 Summary of Current Knowledge

Synthetic aperture radar, SAR, is a type of radar capable of producing a high resolution ground map of an area. SAR uses the platform's relative motion with respect to the ground to synthesize or artificially create a very large aperture. This aperture synthesis overcomes the physics of real beam radar resolution which limits the resolution possible for a given system. Polarimetric SAR completely characterizes the reflectivity of a region by transmitting and receiving both horizontally and vertically polarized pulses at the same time. This provides enhanced texture sensitivity measurements of the surface. The recent development of a few high resolution polarimetric SAR systems has created a tremendous amount of research aimed at taking advantage of the total phase characterization of the surface.

For a computer to take a SAR image and locate potential targets, some method of finding the areas of interest in the scene is needed. The process of locating areas of interest is known as segmentation. Humans are extremely good segmenters. They can look at a scene and immediately locate areas of interest. To date, computers have not been successful at quickly segmenting a scene. They are extremely good correlators or template matchers. However, template matching with a large database of templates is very time consuming and requires an accurate computer model of the target of interest. Since it is impossible to know the exact orientation and aspect angle of the target being imaged beforehand a large number of templates must be searched through for correlation to be successful. Specific target characteristics can be difficult to obtain, a complete template library may be difficult to generate.

Many different types of segmentation algorithms exist. These segmentation algorithms fit into two basic categories: discontinuity and similarity. The first category uses abrupt changes to distinguish between regions of interest. Thus, in this category, discontinuities are processed to detect isolated points, lines and edges in an image. In the second category, the similarity between pixel values are used to perform thresholding and region growing. Researchers using these traditional tech-

niques have been unable to develop the perfect segmenter (7:331).

Recently, a new field of mathematics, Fractal Geometry, has emerged that may provide an answer to this segmentation problem. The applicability and potential of fractal analysis to image segmentation has been demonstrated (20, 11, 14). Captain Maneely demonstrated the ability of fractal dimension estimation to segment coarse resolution (10 meter impulse response) polarimetric SAR imagery. Maneely's research showed that fractal dimension estimation could be used to separate areas of high cultural concentration (i.e. cities) and natural regions (14:6–1).

1.4 Scope

This thesis details an approach to distinguish automatically between four classes of regions (culture, tree, field, shadow) within a high resolution SAR image. The data used during this thesis effort were from the Massachusetts Institute of Technology Lincoln Laboratory (MIT/LL) Advanced Detection Technology Sensor (ADTS). The ADTS is a polarimetric SAR operating at 33.56 GHz, capable of collecting one foot resolution images in the range and cross–range directions. The radar alternately transmits horizontally and vertically polarized pulses and has the ability to receive both polarizations simultaneously. The complete polarization scattering matrix (PSM) is collected using this system (17:3-4).

The data used were identified from a clutter data base. Detailed ground truth of the imagery was not available. However, for the majority of the SAR imagery used, corresponding aerial photography was available.

All combinations of the linear polarimetric data contained within the PSM were evaluated to determine which combinations of the data provided the best segmentation results.

1.5 Assumptions

The following two basic assumptions were made:

- Fractals model nature. Scientists in many disciplines adopt this as scientific fact (19:25).
- The SAR image formation process is linear. Fractal dimension is constant across a linear transformation of a data set (2:180). With this assumption, the fractal dimension of the surface can be estimated from the SAR image. Alex Pentland, in his article "Fractal Based Description of Natural Scenes," found that "we can estimate the fractal dimension of the surface by measuring the fractal dimension of the image data" (20:187).

1.6 Approach

The objective of this thesis is to answer the following questions:

- Can fractal geometry be used to effectively segment high resolution polarimetric SAR imagery into natural and cultural regions?
- Do naturally occurring regions within a SAR image exhibit values of fractal dimension that can be used to separate between the regions?
- Does the use of polarimetric SAR data instead of non–polarimetric data improve the ability to segment images using fractal dimension estimation?
- Can an artificial neural network be trained using multiple fractal dimension images as features to distinguish automatically between different regions within a SAR image?

These questions were answered by investigating the potential to segment one foot resolution SAR imagery using correlation dimension estimation, a method of estimating fractal dimension. After estimating the correlation dimension of SAR imagery, standard image processing techniques were applied to determine if correlation dimension estimation provided useful features for segmenting SAR imagery. Also, both supervised and unsupervised neural networks were trained using correla-

tion dimension estimates as input features to evaluate the applicability of correlation dimension estimates as input features for segmenting SAR imagery.

Details of the correlation dimension estimation process and the neural network implementations are contained in the methodology chapter of this thesis.

1.7 Hardware and Software Requirements

The intent during the course of this research was to develop the software tools and programs necessary to estimate correlation dimension and segment SAR imagery independent of computer system being used. All programs were written in C, a highly portable language. The programs were validated to insure identical results UNIX and DOS operating systems. The following computer systems were used during the course of this research effort:

- Sun Sparc 1+ using SunOS v4.01
- C Language Compiler
- ADOBE Photoshop
- 386–MATHLAB^{tm} Software Package
- SUN 3/160 Workstation using SunOS v4.0.3
- 386 Based computer with 80387 Math co–processor using DOS V4.01 Operating System
- Turbo C V2.0 Integrated Development Environment

1.8 Sequence of Presentation

Chapter II presents the topic of Fractal Geometry. It covers fractals, image segmentation using fractal geometry, and the application of fractal dimension estimation to SAR imagery.

Chapter III contains the thesis methodology. In this chapter the description and justification of the fractal dimension estimation algorithm are discussed. The neural network implementation and training details are also presented.

Chapter IV contains the analysis of the implementation and the results obtained.

Chapter V is the conclusion. It presents this researcher's conclusions and recommendations for further research.

1.9 Summary

In this chapter the need for performing segmentation on SAR imagery was introduced. Traditional image processing techniques have been unsuccessful at developing robust segmentation algorithms. This thesis effort is directed at increasing the knowledge about fractal dimension measurements of polarimetric SAR data.

II. Fractal Geometry

2.1 Introduction

> In our description of nature the purpose is not to disclose the real essence of the phenomena but only to track down, so far as it is possible, relations between the manifold aspects of our experience (4:18).

In 1934, Niels Bohr, in his book *Atomic Theory and the Description of Nature*, stated the prevailing belief among scientists that nature was impossible to describe. That was true using classical geometry. However, in 1975 Benoit Mandelbrot described a "Geometry of Nature" that would be able to handle the description of natural creations. Fractal geometry was born out of the frustration of trying to describe the shape of a cloud, a mountain, a coastline, or a tree (13:1-5). Once the language of fractal geometry is mastered, natural objects can be described as easily as artificial objects (2:1).

2.2 Overview

The purpose of this chapter is to present the topic of Fractal Geometry. First, fractals will be introduced. Next, image segmentation using fractal geometry is discussed. Finally, the application of fractal dimension estimation to Synthetic Aperture Radar (SAR) data will be presented.

2.3 Fractals

Euclidean geometry failed when it came to describing irregular shapes. By conceiving and developing a new field of mathematics, "Fractal Geometry," Mandelbrot was able to overcome the limitations of topological dimension imposed by classical geometry where a point has zero dimension, a line one dimension, a plane two dimensions, and space three dimensions (6:96-97). The term fractal dimension

is a generic term that has been used to describe any dimension that is not characterized by an integer (28:9). A fractal dimension "agrees with our intuitive notion of dimension (30:1)."

> A fractal is by definition a set for which the Hausdorff Besicovitch dimension strictly exceeds the topological dimension. (13:15)

Or $D_f > D_T$, where D_f is the Hausdorff Besicovitch or "fractal" dimension, and D_T is the topological dimension.

Understanding the concept of self–similarity or scaling will provide the basis for gaining an intuitive feel for fractals and fractal dimension. Consider a line segment as shown in Figure 1. Scaling it down by a ratio, r=1/N, from the whole yields N identical line segments. The same holds true for a square in a plane and a cube, scaling them down by a ratio, $r=1/\sqrt{N}$, or $r=1/\sqrt[3]{N}$, respectively, yields N self-similar objects either squares or cubes. Generalizing, $r=1/\sqrt[D]{N}$ for a D–dimensional self–similar object that has been scaled by a factor r. Thus, solving for D yields (19:28-30):

$$D = \frac{log(N)}{log(\frac{1}{r})} \tag{1}$$

D = Dimension

N = Number of self-similar subintervals

r = Length of each sub-interval

This property of self–similarity is what forms the basis for fractal geometry (19:28-30).

Any object that has the property of self–similarity is said to be a self-similar fractal. An analogy of a self–similar fractal that is immediately recognizable to most Americans is one of a Wheaties^{tm} box with a picture of someone sitting down at a table with a Wheaties^{tm} box that has a picture of someone sitting down at a

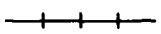

1-D N-Parts, scaled by ratio $r = \frac{1}{N}$

$$Nr^1 = 1$$

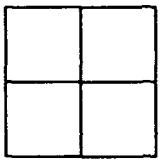

2-D N-parts, scaled by ratio $r = \frac{1}{\sqrt{N}}$

$$Nr^2 = 1$$

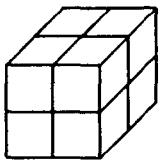

3-D N-parts, scaled by ratio $r = \frac{1}{\sqrt[3]{N}}$

$$Nr^3 = 1$$

GENERALIZE

For an object of N parts, each scaled down by a ratio r from the whole

$$Nr^D = 1$$

defines the fractal similarity dimension D

$$D = \frac{log(N)}{log(\frac{1}{r})}$$

Figure 1. Dimension Determination of Self-Similar Objects (19:29)

table with a Wheaties^{tm} box (28:3). Viewing the picture of the Wheaties^{tm} box at different scales results in exactly the same image. By definition, using classical geometry, dimension is an integer. In fractal geometry, D does not have to be an integer (13:15). Thus, in Equation 1, D can be replaced with D_f, resulting in an equation for fractal dimension. Fractal dimension gives a more intuitive feel for the concept of dimension, an indicator of the *roughness* or *wiggliness* of a surface. It provides a method for quantifying natural shapes (30:6-8).

In the last 15 years, since the beginning of fractal geometry, fractals have become an integral part in most fields of science (30:3). The ability of fractals to describe natural phenomena has led to their use in a wide range of applications. In his book *Fractals Everywhere*, Barnsley demonstrates the ability of fractals to model natural objects. Fractal geometry has been applied to "biological modeling, physiological modeling, geography, coastlines, turbulence, images, computer graphics, feathers, and ocean spray" (2:backcover).

Fractals in nature are not strictly self–similar. They are statistically self–similar, meaning they look statistically similar while at the same time they look different in detail at different length scales over some finite range. The concept of fractal dimension can still be applied to statistically self–similar objects. Some fractals demonstrate a property known as self–affinity, where the fractal is scaled by different scaling factors in each direction (2:43-57). Objects possessing self–affinity introduce difficulties in determining the fractal dimension. (30:19)

2.4 Image Segmentation

When considering the standard pattern recognition problem of finding an object in a scene there are two main approaches. The first approach is processing the image in such a way as to locate the object of interest directly using template matching. The second, and more common approach, is to segment the image into areas of interest using image processing techniques, such as thresholding and edge

enhancement, then to perform a second level of processing to find the object.

> Segmentation is one of the most important elements in automated image analysis because it is at this step that objects or other entities of interest are extracted from an image for subsequent processing, such as description and recognition (7:331).

The applicability and potential of fractal analysis to aid in image segmentation has been demonstrated (20, 11, 14). By measuring the fractal dimension of an image, the fractal dimension of a surface can be estimated. Pentland demonstrated the ability of fractal analysis to segment an image and yield useful pattern recognition results (20:661-674). The basis for using fractal dimension as a feature set for image segmentation is that man–made objects are usually not fractal in nature. Manufactured objects do not exhibit a fractal dimension that is stable, where stable is defined as a fractal dimension estimate that is the same over a large range of scales. Most artificial objects are smooth in contrast to natural objects which exhibit a roughness at all scales of inspection. The smoothness of artificial objects tends to produce a low and unstable fractal dimension.

Fractal dimension estimation techniques were applied to L–band (24 cm) polarimetric SAR data by Maneely in order to facilitate segmentation. Using fractal geometry he was able to segment coarse resolution (10 meter impulse response) SAR imagery into natural regions and cities. Taking advantage of the added information available from polarimetric data provided better segmentation capabilities than using straight magnitude information alone (14:6.1-6.2).

2.5 Measuring Fractal Dimension

By applying Equation 1, we are able to determine the fractal dimension of the four shapes in Figure 2. Each of these shapes exhibits exact self–similarity. Note that as D_f approaches 2 from 1 the shape approaches a plane. This equation can be extended to higher dimensions. For example, if Equation 1 was extended to

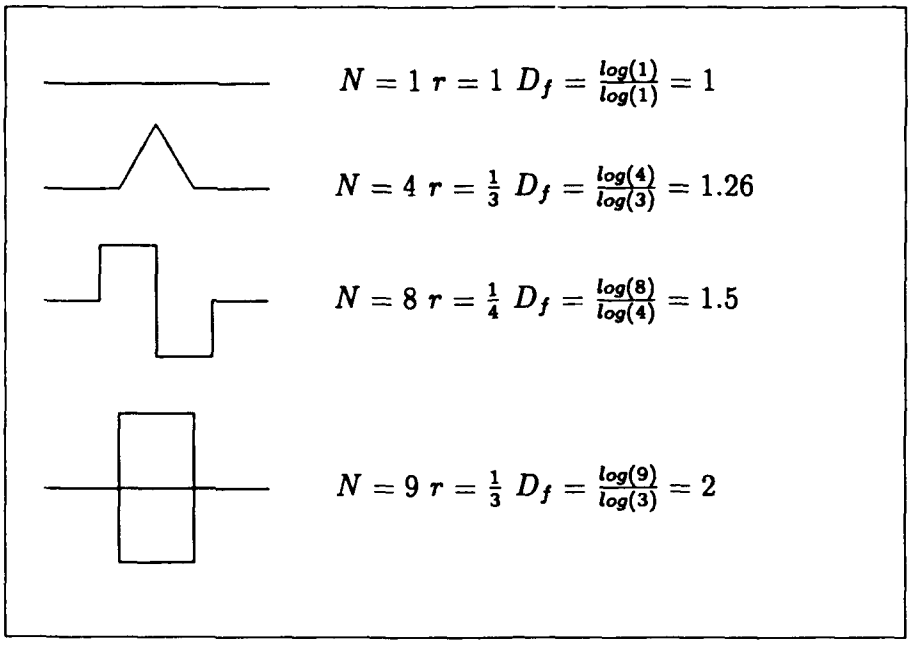

Figure 2. Fractal Dimension Estimation (19:27)

two–dimensional euclidean space rather than counting line segments, box counting would be used. Extending to euclidean three–dimensional space would mean cubes would be counted (19:61-62). This method is relatively easy to implement and for low dimensional fractal sets can be quite useful. However, implementing a box counting algorithm can be computationally very expensive (28:17). To get a feel for the amount of computer capacity required to implement the box counting algorithm consider that the number of cubes increases exponentially with the fractal dimension $N(l) = l^{-D_f}$. The size of the cubes must be small enough to insure asymptotic scaling has been reached. Thus applying typical numbers $D_f = 3$ and $l = .01$ then N is approximately 10^6. Implementing a box counting algorithm to estimate fractal dimension for high dimensional fractals is impractical (28:17).

A polarimetric radar produces a full polarimetric scattering matrix consisting of four complex elements denoted HH, HV, VH, and VV. These complex elements are collected by first transmitting a horizontally polarized signal and receiving two orthogonal polarizations denoted HH and HV. Next, a vertically polarized signal is

transmitted and the two polarizations are received and denoted VH and VV. This process is repeated, alternately transmitting horizontally and vertically polarized signals. HV is often assumed to be equal to VH by reciprocity, however the data can be distinct for a real radar . The three complex elements HH, HV, and VV comprise the total information in the polarization scattering matrix (17:2).

Starting with radar imagery from a fully polarimetric radar with the intent to extract as much information as possible using fractal geometry leads to the conclusion that a fractal dimension estimation algorithm that can handle a minimum of eight dimensional fractals is required. The eight dimensions would consist of the in–phase and quadrature components of each complex element in the polarimetric scattering matrix. Since the intent is to determine what combination of information from the polarization scattering matrix provides the best segmentation results, a fractal dimension estimator that is capable of easily accepting different dimension fractals as input is required. Because of the large number of pixels contained within an ADTS image (2048 by 512 pixels) and the number of data points for each pixel, a computationally efficient fractal dimension estimator is required. With the above requirements in mind, finding an algorithm to compute fractal dimension of the data set the researcher is led to evaluate several different methods of implementing a fractal dimension estimator. Several different dimension estimates characterize fractals. However, only three truly different dimension estimates, *fractal or similarity*(D_f) (13, 2, 6, 19, 14, 11, 28, 5), *information*(σ) (28, 12, 9, 5, 8), and *correlation*(ν) (23, 12, 9, 28, 26, 27, 8, 3, 24) have been discussed at great lengths in the literature. In their article, *The Infinite Number of Generalized Dimension of Fractals and Strange Attractors*, Hentshel and Procaccia, came to the conclusion "there is an infinite number of different (and relevant) generalized dimensions" that can characterize fractal objects (10:436). Grassberger and Procaccia determined that all three

different dimension estimates are related and in general (9:191):

$$\nu \leq \sigma \leq D_f \tag{2}$$

ν = correlation dimension

σ = information dimension

D_f = fractal or similarity dimension

Grassberger and Procaccia also developed a method for determining the correlation dimension of fractal data that is not computationally intensive and allows the flexibility to process various dimensions of fractal data without extensive software modifications (9:189). Many articles have been written discussing correlation dimension estimation (23, 12, 9, 28, 26, 24, 8, 3, 27). Theiler provides an excellent discussion on correlation dimension, how to implement it, and common sources of error involved in the process of determining correlation dimension (28:12-21).

This researcher decided correlation dimension estimation was the proper path to pursue in search of a fractal geometry approach to segmenting SAR imagery . This decision was made because estimating correlation dimension is not computationally expensive to implement and provides the flexibility required to experiment with numerous combinations of SAR data input (9:189).

2.6 Summary

Fractal Geometry has drastically changed the way scientists look at the world. It is no longer impossible to describe and model nature. Fractal dimension estimation techniques have proven useful in such diverse fields as biology, physiology, topology, and computergraphology. Measuring the fractal dimension of sensor imagery has

been proven to be a useful technique for determining the fractal dimension of nature itself. Fractal dimension estimation offers an alternate means of segmenting high resolution synthetic aperture radar polarimetric data.

III. Methodology

3.1 Introduction

This chapter describes the approach and methodology used during this thesis effort to investigate the potential of correlation dimension estimation to segment polarimetric SAR imagery. The chapter begins with a review of the objectives of this thesis and an overview of the approach taken to answer these questions. Following the overview, a description of the polarimetric radar collection system and the data it produces will be provided. After describing the data, correlation dimension estimation is introduced and the approach taken to apply the correlation dimension estimation process to polarimetric SAR imagery is presented. Then, the procedure used to evaluate the resulting correlation dimension image is discussed. Finally, details of two different artificial neural network systems implemented to distinguish automatically between different naturally occurring regions will be examined.

3.2 Overview

The goal of this thesis was to determine if correlation dimension estimates are valid features for use in segmenting SAR imagery. The first objective was to determine if correlation dimension estimation of SAR imagery could be used to distinguish between naturally occurring regions and man–made regions. Secondly, could correlation dimension estimates be used to distinguish between different naturally occurring regions such as tree, field and shadow. Other thrusts of this research were in the following two areas:

Polarimetric SAR How does using polarimetric SAR data affect the correlation dimension estimation? Do multiple polarizations aid in segmentation?

Neural Network Can an artificial neural network be trained to segment SAR imagery automatically using correlation dimension estimates as features?

3.3 Approach

Shown in Figure 3 is a block diagram of the methodology. Each SAR image consisted of In-phase (I) and Quadrature (Q) components corresponding to each pixel in the image. The first step taken was to convert the SAR image data into UNIX format. A C program DETECT.c was executed to convert the I and Q components into magnitude values for display. Aerial photographs, ground photographs, and any other available ground truth documentation of the imaged sites were used to produce image truth templates from the displayed SAR images. These image truth templates were considered to be an accurate representation of the SAR image and as such were used to evaluate the accuracy of the resulting segmented images.

FRACTAL.c was the program used to produce correlation dimension images from the input SAR images. The approach taken was to sub-divide the SAR image into non-overlapping regions (windows). The correlation dimension, (ν), of each window was calculated based on window size, the distance calculation parameter, and polarization combination. Window size ranged from 4×4 to 16×16. Magnitude, Phase, both Magnitude and Phase, and I and Q were used as parameters for determining which components to used for distance calculations. The polarization combinations used were the fifteen different combinations of the four elements in the PSM (HH, HV, VH, VV, HH & HV, HH & VH, HH & VV, HV & VH, HV & VV, VH & VV, HH & HV & VH, HH & HV & VV, HH & VH & VV, HV & VH & VV, HH & HV & VH & VV). The result of calculating the correlation dimension for a particular combination of polarizations was a file containing one correlation dimension estimate for each window of the original SAR image. This resulting file is referred to as a correlation dimension image.

After creating the correlation dimension image, two separate approaches were taken to evaluate the potential of using correlation dimension estimates for segmenting SAR imagery. The first approach was using standard image processing techniques (thresholding, median filtering) to produce segmented images. In the second

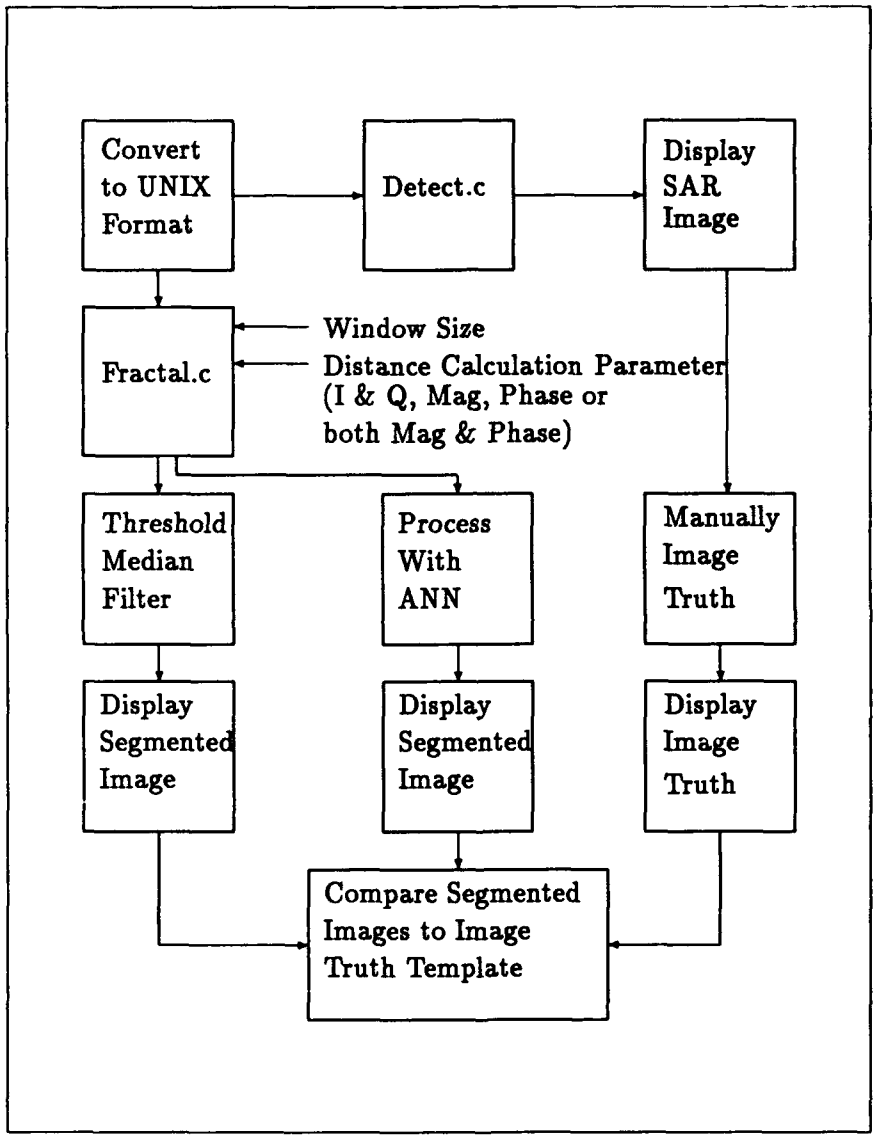

Figure 3. Block Diagram of Methodology

approach, two different types of artificial neural networks (ANN) were trained using multiple correlation dimension images to obtain correlation dimension estimates as input features to produce segmented images. The two ANNs used were the Kohonen, an unsupervised ANN, and a radial basis function (RBF), a supervised ANN. The segmented images produced by the two approaches were then compared pixel by pixel to the image truth template to evaluate the accuracy of the segmentation.

The majority of this thesis work was performed using the UNIX operating system on SUN workstations. However, two other computers running the UNIX operating system were used to execute batch jobs of the correlation dimension estimation software. These systems were the AFIT ELXSI 64 systems (Galaxy and Orion). VMS was used only when necessary to convert data into a format usable by UNIX. All C programs were also converted to run on DOS systems using Turbo C by Borland.

3.4 Advanced Detection Technology Sensor

The Advanced Detection Technology Sensor (ADTS) is a 35 GHz monostatic synthetic aperture radar system developed for Defense Advance Research Project Agency by Massachusetts Institute of Technology Lincoln Laboratory (MIT/LL). ADTS is a coherent and fully polarimetric calibrated SAR system. The resolution used during this research effort was one foot in both range and azimuth. The polarimetric data for a particular scene consists of four files corresponding to the four complex elements (HH, HV, VH, VV) from the polarimetric scattering matrix (PSM). The first letter in the identifier of the elements of the PSM corresponds to the polarization of the transmitted signal and the second letter corresponds to the polarization of the received signal. For example, HH signifies the horizontally polarized transmitted signal received with a horizontally polarized antenna.

The data used consisted of the I and Q components of each polarization in 8-8-4 compressed format and stored on 2.3 Gigabyte 8 mm Exabyte Tape using the

VMS operating system (16). Appendix A describes the procedure used to convert the 8-8-4 compressed data into a UNIX float format file containing the I and Q components alternately. In order to view the imagery, a C program, DETECT.c, was executed on the UNIX float format files. DETECT.c calculates the magnitudes from the I and Q values and then logarithmically scales the magnitudes between 0 and 255 before creating an unsigned byte output file. These unsigned byte files could then be viewed using standard image processing software available on the SUN workstations or Macintosh systems.

3.5 Data Sets

MIT/LL has collected a large database of ADTS clutter data from various sites around the country. ADTS clutter data was collected in order to study the characteristics of background clutter from different regions of the country. The ADTS data available for this research was clutter data collected in New York, Maine, and Minnesota. Initially, the goal was to process a large number of images in order to get a statistically valid evaluation of correlation dimension segmentation capabilities. Typically, when no specific targets are contained within the clutter imagery, detailed ground documentation, ground truth, is not available.

One foot resolution was thought to contain the detail necessary to image truth the imagery directly from the ADTS image without additional ground truth documentation. ADTS imagery was to be used to provide image truth as to what was actually in the scene. However, during the image truth process, corresponding aerial photography of a portion of the data was obtained. After comparing the aerial photo with image truth templates that had been generated using only the SAR imagery, it was observed that image truthing without proper ground truth was impractical. Shown in Figure 4 is an example of an ADTS image that is difficult to image truth using the SAR image alone. There was a large portion of Mission 98 Frame 08 that contained a tree farm. The tree farm is not clearly visible in the ADTS image. How-

ever, the tree farm can be observed by viewing the aerial photograph corresponding to Mission 85 Frame 08 shown in Figure 5. Thus, the imagery presented in this thesis is a subset of the larger set processed and was selected because of additional information (i.e. aerial or ground photographs, site sketches) to support image truthing. Even with aerial photography of the scenes it is still a difficult task to image truth an image without detailed ground truth measurements.

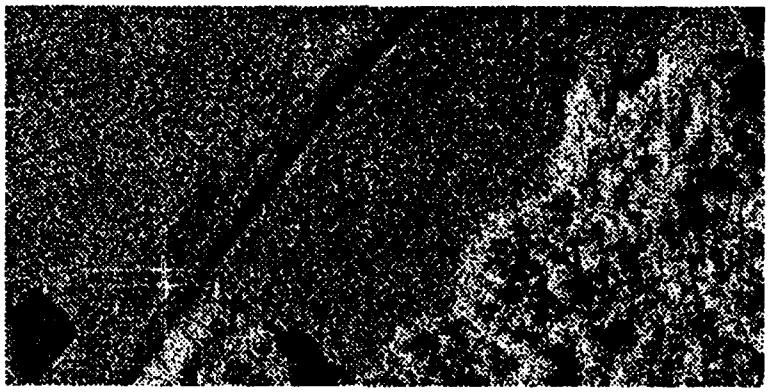

Figure 4. M98F08 HH Polarization 1024 × 512

Figure 5. Aerial Photograph M98F08

The original SAR image frames were 2048 × 512 pixels. These frames contained low amplitude return areas on both the left and right side of the image due to the roll–off of the main beam of the radar. Correlation dimension estimation is based on relative amplitudes between pixels within a single window. Because of the scaling

that occurs before estimating the correlation dimension for a particular window, the correlation dimension estimates appear to be valid in this low return area. However, the radar is calibrated for the center of the main beam. The low values on both sides is uncalibrated and solid conclusions could not be drawn from this region. Thus, the center 1024×512 pixels from each frame, corresponding to the calibrated region of the frame, were used during this research.

3.6 Calculation of Correlation Dimension

As discussed in the previous chapter, there are several different methods of calculating fractal dimension. The method implemented during this research was the correlation dimension estimation introduced by Grassberger and Procaccia (9:189–208). This method estimates the dimension based on the statistics of pairwise distances (28:13).

The correlation dimension (ν) as defined by Grassberger and Procaccia is given as:

$$\nu = \lim_{r \to 0} \frac{\log C(r)}{\log r} \tag{3}$$

The definition of the correlation integral is:

$$C(r) = \lim_{N \to \infty} \frac{1}{N^2} \sum_{\substack{i,j=1 \\ i \neq j}}^{N} \theta(r - ||\vec{X}_i - \vec{X}_j||) \tag{4}$$

where:

N is the number of points in the data set

$\theta(x)$ is the Heaviside unit step function

$||\vec{X}_i - \vec{X}_j||$ is some distance metric between $\vec{X}_i and \vec{X}_j$ (i.e. euclidean distance)

r is variable corresponding to range of distance measurements

The method was originally used to estimate the dimension of time series data using

large numbers of data points. In order to implement this method, the distance via some metric (i.e. euclidean distance) between every vector combination representing time series data is calculated. After performing distance calculations, the number of distances C(r) less than r, as r is reduced from the maximum distance to zero, is determined. C(r) and r are plotted on a log–log plot and the slope is an estimate of the correlation dimension estimate. Assuming that amplitude variation from a homogeneous region of SAR imagery is analogous to multiple samples from time series data, an application of the correlation dimension estimation method to imagery data results. Multiple polarization information can be included for each pixel location by simply expanding the vector used to describe each pixel.

Several interesting questions arose when attempting to implement this procedure for calculating the correlation dimension of SAR imagery.

The first was whether the x and y location of each pixel should be included in the distance measurement. Since each sampled window would have the same underlying grid structure could the grid structure be ignored, thus eliminating bias caused by the grid structure? The x and y coordinates were not included, since the pixels were considered analogous to time series data and time difference between different time samples were not included in the distance measurement for time series data.

The next dilemma encountered was the representation of the input data that should be used to calculate the euclidean distance between points. The choices were using 1) the I and Q components of each polarization, 2) the magnitude and phase information separately or 3) the magnitude and phase simultaneously. Either magnitude and phase or I and Q provide a complete description of the polarimetric data available. This question was an open issue during the course of this research and thus correlation dimensions were calculated using both I and Q, magnitude, phase, and a combination of both magnitude and phase.

The optimum size of window to use for correlation dimension estimation was

Table 1. Calculation of Correlation Dimension

For Each Subregion Perform The Following	
Step 1	Read in I and Q information corresponding to each pixel for each polarization desired
Step 2	Calculate Magnitudes and Phases
Step 3	Find Maximum Magnitude
Step 4	Scale Magnitudes or I and Q data based on $\frac{Window-Size}{max-magnitude}$ and calculation parameter being used I & Q, mag, phase or both mag and phase
Step 5	Calculate euclidean distance between each pixel in a sub-region and every other based on calculation parameter
Step 6	Count number of distances less than r as r is reduced to zero
Step 7	Calculate slope via weighted least squares method for log C(r) vs log r
Step 8	Slope is Correlation Dimension Estimate

an engineering trade-off. The larger the window size the better the statistical estimation of correlation dimension. However, since the goal was to segment SAR imagery into different naturally occurring and cultural regions it was necessary that the window sizes be small enough to isolate a specific type of background region. These conflicting requirements lead to an investigation of window sizes ranging from 4×4 to 16×16.

The procedure for calculating the correlation dimension for individual subregions of a SAR image is given in Table 1.

3.7 Viewing Correlation Dimension Estimates as Imagery

After the correlation dimension was estimated for each polarization and combination of polarizations, each file containing the correlation dimension estimates

was converted to unsigned byte format and displayed as an image. Thresholds were set to separate between different correlation dimension values in the resulting image. When the image contained large regions of either field, tree, or shadow, a median filter was applied to reduce noise within the image. Median filtering after setting the threshold to separate culture was not applied since many of the culture objects identified were small (i.e. corner reflectors, farm vehicles). These items occupied only one window and a median filter operation would eliminate that window entirely. After thresholding and median filtering correlation dimension values for each of the four classes, each class was assigned a particular grayscale value. The resulting segmented correlation dimension image was then compared to the corresponding image truth template in order to evaluate how accurately the regions identified by correlation dimension estimation matched with the image truth template.

3.8 Artificial Neural Networks

Two different types of neural networks were used to investigate the potential of combining multiple correlation dimension images into one segmented image. The two types of neural networks used were the Kohonen, an unsupervised network, and the radial basis function, a supervised network. This section will provide an overview of the two neural networks used.

3.8.1 **Kohonen Neural Network** A Kohonen neural network is a type of neural network capable of taking input vectors and clustering them into regions of similarity. This is done in an unsupervised mode meaning a large number of training vectors are applied to the training net and the Kohonen network adjusts weights in such a way as to cluster the data into different classes. This will only work if the input data are separable. After completing training, the weights from the training net are used to build a new network. It is necessary at this time to calibrate the new network by applying vectors of known types and determining which nodes on the output surface correspond to that particular type of data. If there is a separation

on the output surface between different types of input data then the network can be used to classify test data.

A Kohonen training network that has been developed over the course of several years by AFIT students, primarily Recla and Barmore, was used as the training net to obtain the weights required to implement the neural net requiring calibration for SAR image segmentation (21, 1). Shown in Figure 6 is the Kohonen architecture implemented by Recla and Barmore. The code for this network was written in C for the VMS operating system. The code was modified to run on both UNIX and DOS operating systems. The Kohonen training net written by Recla and Barmore is menu driven and provides the capability to apply the following gain reduction methods:

- Linear Type #1
- Piecewise Linear
- Linear Type #2
- Exponential
- Central–Adaptation
- Exponential/Central–Adaptation

Details of the various gain reduction methods are covered by Barmore and Recla (21, 1). This Kohonen network has the capability of handling 16 inputs and producing an output layer up to 20×20. Conscience can also be used.

A program (NEWNET.c) was written to take the weights from the training network and produce the output Kohonen layer for a given input. The output node values were scaled between $0 - 1$ in order to determine quickly the winning node or nodes. The node with the lowest value (i.e. zero) is considered to be the winner.

The input data used to train the Kohonen neural network was the correlation dimension values obtained from correlation dimension images generated from various

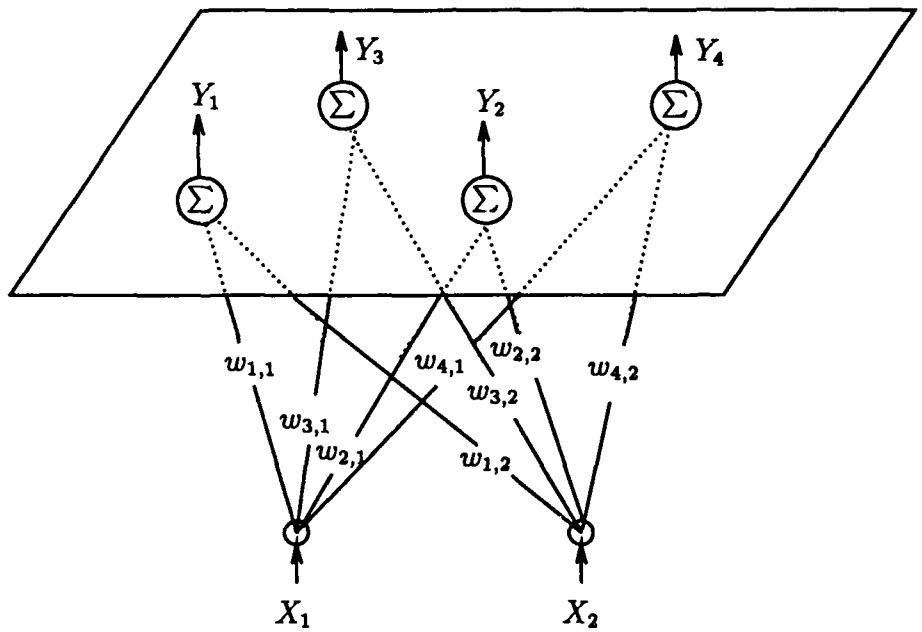

OUTPUT: $Y_j = \sum(X_i - w_{i,j})^2$

TRAINING: $w_{i,j}(t+1) = w_{i,j}(t) + \alpha(t)(X_j(t) - w_{i,j}(t))$

Figure 6. Kohonen Neural Network Architecture (25:19)

combinations of polarizations from the PSM. The net was then calibrated by determining regions on the original SAR imagery that contained a specific type (i.e. field, tree, shadow, culture) region and identifying which nodes on the output Kohonen layer correspond to that particular type of data.

After calibration, a file containing vectors corresponding to correlation dimension estimates from an entire SAR frame is applied to the calibrated network. The output of the net is a grayscale image whose values represent the class of the winning nodes. This output image is then compared to the image truth template to evaluate the similarity of the segmented image with the image truth template.

3.8.2 **Radial Basis Function** Radial basis functions (RBF), according to Moody and Darken (15:133), are a departure from the traditional McCullough and Pitts neuron. A McCullough and Pitts neuron provides for summation of vector inputs through a threshold device to determine the boolean output. The radial basis function neuron represents localized Gaussian overlap regions. Their activation is provided by placement of the Gaussian centers (mean) and establishment of its inclusion region (standard deviation). Research performed by Moody and Darken used radial basis functions for prediction of the Glass-Mackey time series. Moody and Darken point out that RBFs require less training time while still achieving accuracy equivalent to the multi-layer perceptron (15:140).

RBF networks are trained in a supervised mode. As opposed to the Kohonen network, the RBF network requires knowledge of the class for each training vector.

The RBF network implemented during this research was developed by Dan Zahirniak (31). Shown in Figure 7 is the RBF architecture implemented by Captain Zahirniak. The network consists of an input layer, a hidden layer, and an output layer. The hidden layer nodes used the Gaussian function as the RBF. Shown in Figure 8 is an example of a two–dimensional RBF. The centers of the RBF can be set in several different ways. Captain Zihirniak's network was capable of setting the

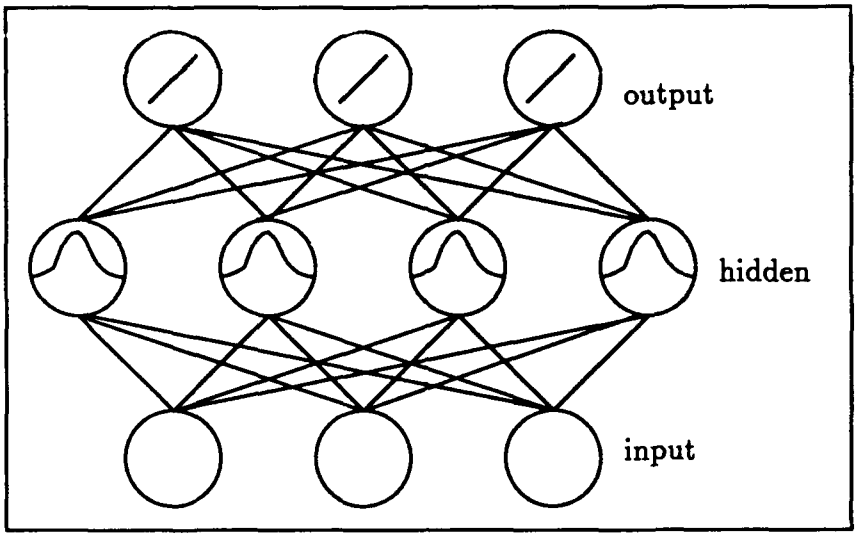

Figure 7. Radial Basis Function Network (18:3)

locations of the center with any of the following rules (31:3-19):

- Nodes at Training Points
- Kohonen Training
- K–Means Clustering
- Center at Class–Cluster Averages

In addition to setting the location of the RBFs the sigmas of the RBF could also be determined based on the following rules:

- Set equal to a constant
- P–Neighborhood Averages
- Scale according to Class Interference

One hundred training vectors from each class of data were used to train the RBF. Because of the limited amount of cultural objects contained within the available

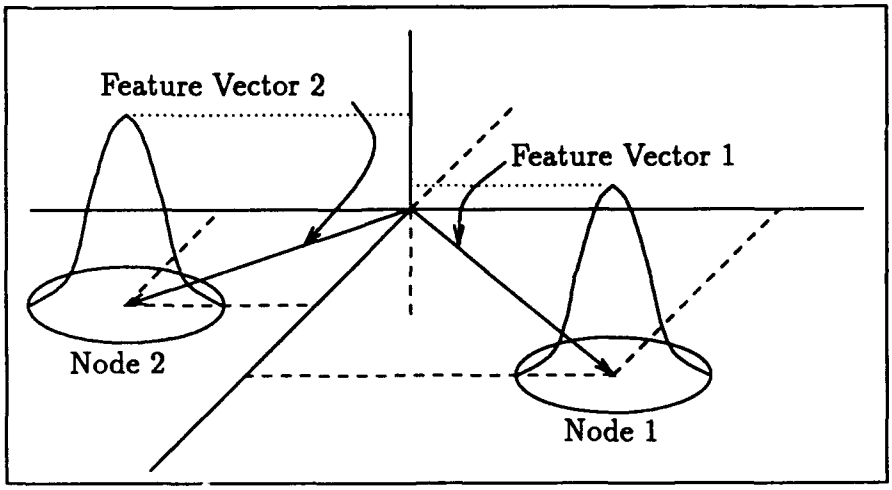

Figure 8. Example of a Two-dimensional RBF (29:34)

imagery, the RBF was trained to identify only the three major naturally occurring regions present in the ADTS imagery (tree, field, shadow). One hundred training vectors from each of the three region classes were used to train the RBF. The training vectors were comprised of correlation dimension estimates taken from corresponding windows of different correlation dimension images. After training the RBF network, a file containing input vectors from an entire image is applied to the network. The resulting file is the grayscale segmented image. This segmented image is compared to the image truth template to evaluate the accuracy of the segmentation process.

3.9 Summary

This chapter described the thesis methodology. The correlation dimension was estimated for different window sizes of the polarimetric SAR imagery. These correlation dimension estimates formed correlation dimension images which were processed via standard image processing methods and neural network implementations to form segmented images. These segmented images were compared to image truth templates

to evaluate the accuracies of the different segmentation methods. Presented in the next chapter are the results of this approach.

IV. Results

...Test Everything; Hold Fast What Is Good ...
Paul's First Letter to the Thessalonians 5:21

4.1 Overview

The results obtained during the investigation of this thesis effort are presented in this chapter. The chapter begins with a quick review of the correlation dimension image formation process. Following that, descriptions of the SAR scenes and image truth templates used during this thesis are provided along with a subjective evaluation of the accuracy of the image truthing. Next, an analytical and subjective evaluation of the correlation dimension segmentation process using only simple thresholding and median filtering on each correlation dimension image will be presented. Finally, the results of fusing various combinations of correlation images via artificial neural networks to produce a final segmented image will be presented.

4.2 Correlation Dimension Image Generation

The original SAR image (1024×512) was divided into non-overlapping windows and the correlation dimension was estimated for each window using every polarization and combination of polarizations. This resulted in fifteen different correlation dimension images corresponding to the fifteen different combinations of components from the polarimetric scattering matrix being created for each SAR frame. In this case, a frame consists of four simultaneously collected polarizations from a particular ground region. These correlation dimension images contained correlation dimension estimates that ranged from 1.3 to 2.2.

4.3 Distance Calculation Parameter

As noted in the previous chapters, the SAR data representation either (magnitude and phase or I and Q) providing the best segmentation via correlation dimension estimation was unknown. Initially, magnitude and phase representations of the SAR data were used to calculate the correlation dimension estimate. Correlation dimension images were generated using magnitude only, phase only, and magnitude and phase simultaneously. While there appeared to be some segmentation potential using either magnitude alone or magnitude and phase simultaneously the use of the phase alone displayed no segmentation potential. Figure 9 is the hand segmented image truth template for M98F08. Figures 10 - 12 are examples using magnitude, magnitude and phase, and phase representations of M98F08 to create correlation dimension segmented images. Using the I and Q representation provided correlation dimension estimates that exhibited improved segmentation potential over representations using magnitude and phase. While an exhaustive analytical evaluation of the potential of magnitude and phase representation of SAR imagery was not conducted to support this claim, preliminary investigation indicated that an I and Q representation would provide better segmentation. As a result, the remaining results presented will be correlation images calculated using an I and Q representation.

Figure 9. Hand Segmented Template M98F08

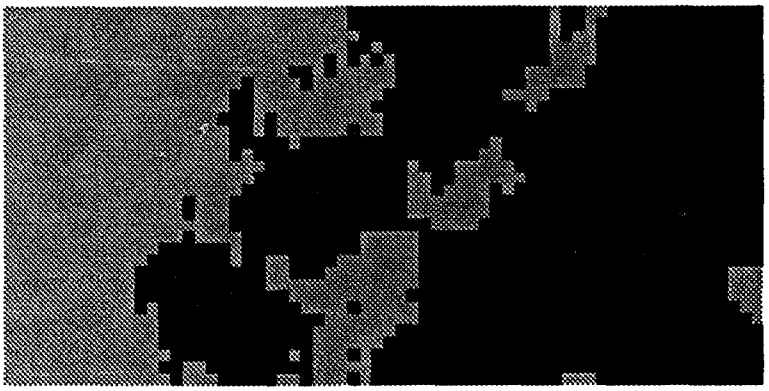

Figure 10. Segmented M98F08 Using Magnitude Values Only All Polarizations WS 16×16

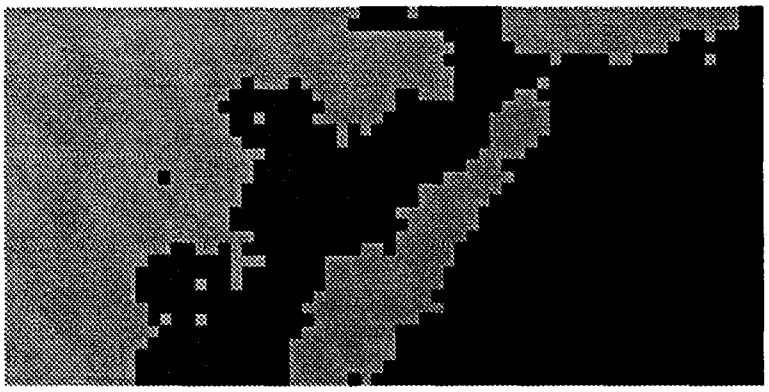

Figure 11. Segmented M98F08 Using Magnitude and Phase Values All Polarizations WS 16×16

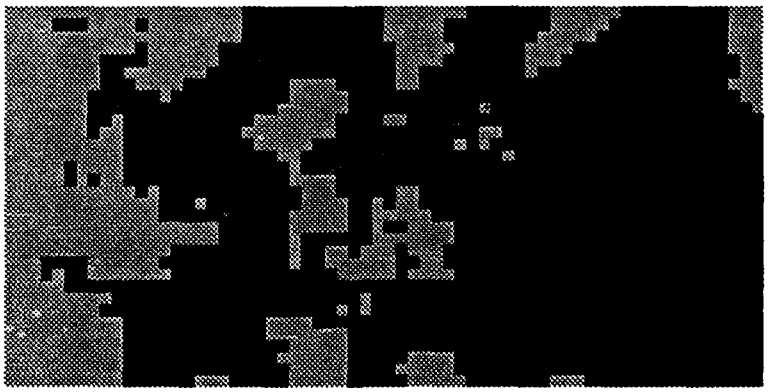

Figure 12. Segmented M98F08 Using Phase Values Only All Polarizations WS 16×16

4.4 Window Size Determination

Window sizes evaluated ranged from 4×4 pixels to 16×16 pixels. The data were one foot resolution in both the range and azimuth direction resulting in a decreased resolution for the correlation dimension image. Thus, starting with an original 1024×512 image using a window size of 16×16 resulted in a 64×32 correlation dimension image representing a 16:1 reduction in resolution (i.e. 16 foot). In the same manner using a 8×8 window size resulted in correlation dimension images that were 128×64. Window sizes of 16×16 and 8×8 provided correlation dimension estimates that exhibited great potential as useful features for segmenting SAR imagery. Using a window size of 4×4 resulted in correlation dimension estimates that were not consistent and robust. Due to the statistical nature of this approach the 16 pixels in the 4×4 window did not provide a large enough sample to be statistically valid. The remainder of this chapter discusses results obtained using window sizes of 16×16 or 8×8.

4.5 ADTS Imagery

This section presents the data the results presented in this thesis were obtained from. The data were from the following two missions:

- Mission 85 Pass 5 Stockbridge, New York Spring 1989
- Mission 98 Pass 3 Portage Lake, Maine June-July 1989

These missions were selected from the large amount of data available due to the accessibility of aerial photography and limited ground truth for these frames. Without detailed ground truth, image truthing of the radar imagery was extremely difficult. Where to draw the borders between tree, field, and shadow regions was not intuitively obvious. More difficult to image truth than naturally occurring regions were regions containing cultural items. With the exception of corner reflectors, accurately image truthing buildings, vehicles, farm equipment, borders between mowed

fields and areas otherwise affected by man's presence was nearly impossible with the ground truth data available. After image truthing a radar image, the 1024×512 image truth template had to be reduced by either 1/16 or 1/8 to produce image truth templates the same size as the segmented correlation dimension images. Cultural items were, in general, smaller than naturally occurring items and this reduction process caused many of the smaller items to disappear. Efforts to correct this problem resulted in image truth templates for cultural items that had locations shifted by one pixel in the image truth template. Thus, the imagery was divided into two different categories 1) imagery containing naturally occurring regions and 2) imagery containing cultural items or regions affected by man's presence (i.e. mowed fields). The following figures present the horizontal transmit horizontal receive polarization of the ADTS SAR imagery used during this thesis effort. Following each image is the corresponding image truth used to evaluate the correlation dimension images and a description of the image providing a subjective evaluation of the accuracy of the image truth. This subjective evaluation of the accuracy of the image truth template is based on the complexity of the scene and the ground truth information available.

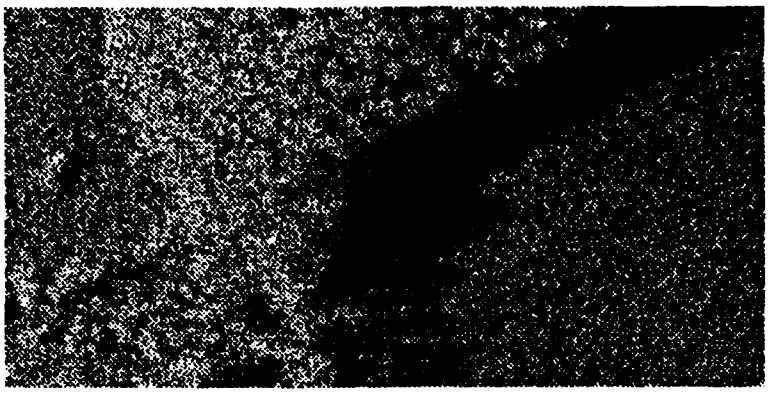

Figure 13. M85F27 HH Polarization 1024 × 512

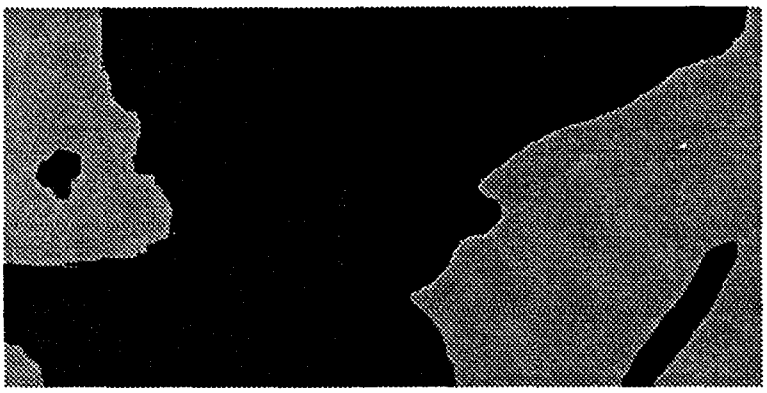

Figure 14. Hand Segmented Template M85F27

4.5.1 **M85F27** This image contains tree, field, and shadow regions. The scattered trees in the bottom left of the image proved difficult to accurately image truth as they were not distinct in the displayed radar image. Also present on the right hand side of this image were ditches not clearly visible when observing the radar image. Creating an accurate image truth template of this image proved to be difficult. Figure 14 is the hand segmented image truth template actually used to analytically evaluate this frame. This researcher estimates the overall accuracy of the template to be approximately 80%. Tree-field boundaries of this template are estimated to be approximately 75% and the accuracy of the tree-shadow and field-shadow boundaries is estimated to be approximately 90%.

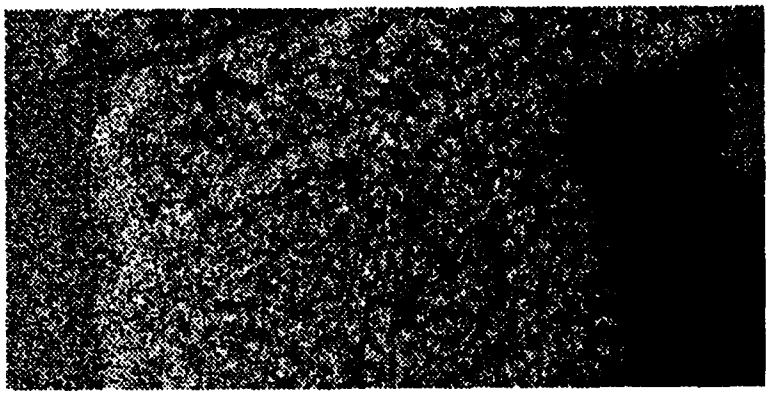

Figure 15. M85F28 HH Polarization 1024 × 512

Figure 16. Hand Segmented Template M85F28

4.5.2 **M85F28** This image contains tree, field, and shadow regions. In addition to the three main regions a dirt road was also present. Since the correlation dimension of a dirt road falls in the same correlation dimension estimate range as trees no attempt was made to image truth the road separately. Few if any scattered trees were present in the image. The estimated tree-field accuracy for this image is approximately 95%. The tree-shadow and field-shadow boundary accuracy is estimated to be 90%. Figure 16 is the image truthed image used to evaluate this frame.

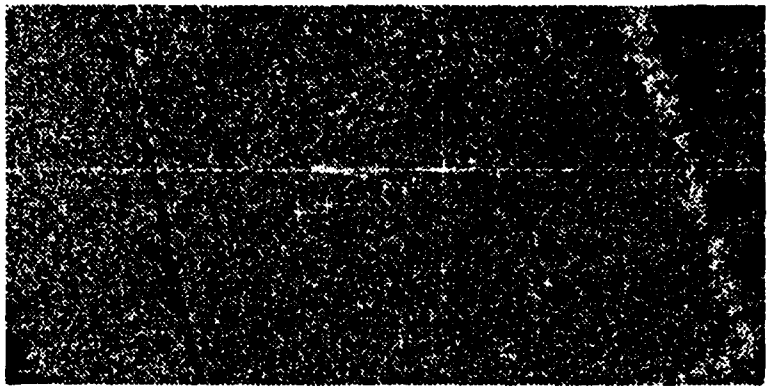

Figure 17. M85F30 HH Polarization 1024 × 512

Figure 18. Hand Segmented Template M85F30

4.5.3 **M85F30** This image contains mainly fields, with a tree line and a road present. In addition, eight corner reflectors and several bent metal poles were present in this image. Presence of the corner reflectors and the metal pole at the middle of the scene were accurately determined as they possessed the largest magnitude values present in the image. Although from ground truth diagrams a metal pole was present near the tree line, but from the SAR image its location could not be accurately determined. Figure 18 is the image truth template of this frame. This scene was not used as part of the analytical evaluation thus no estimated segmentation accuracy is provided.

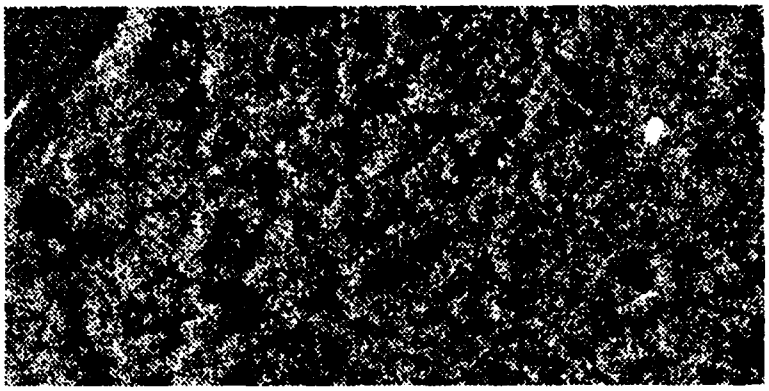

Figure 19. M98F07 HH Polarization 1024 × 512

Figure 20. Hand Segmented Template M98F07

4.5.4 **M98F07** The majority of this image is trees, however, the top left corner of this image contains field. The tree-field boundary is estimated to be at least 97% accurate. This image presented the least difficulty in defining the boundary between the regions. Figure 20 is the template used to evaluate correlation dimension images from this frame.

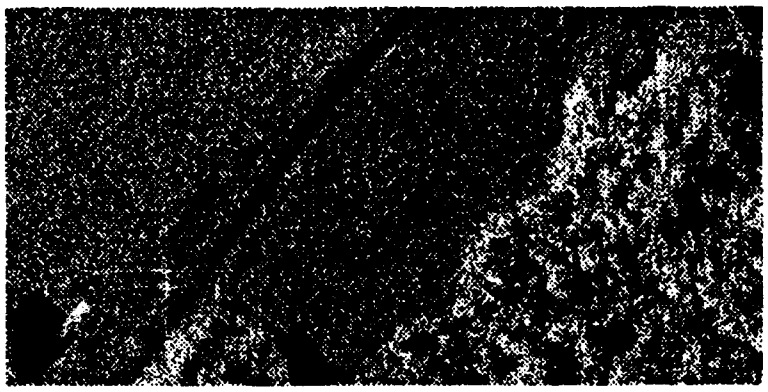

Figure 21. M98F08 HH Polarization 1024 × 512

Figure 22. Hand Segmented Template M98F08

4.5.5 **M98F08** Looking at the SAR image of this frame is very deceiving. Initially this frame was thought to be easily image truthed. The tree-field border looked defined, the pond and the road were darker than the surrounding areas, and the location of the two corner reflectors was determined accurately. However, when aerial photography of this frame was obtained part of the "field" originally defined was actually a tree farm. Using this additional information the image was image truthed to obtain the template shown in Figure 22 with estimated accuracy of 90%.

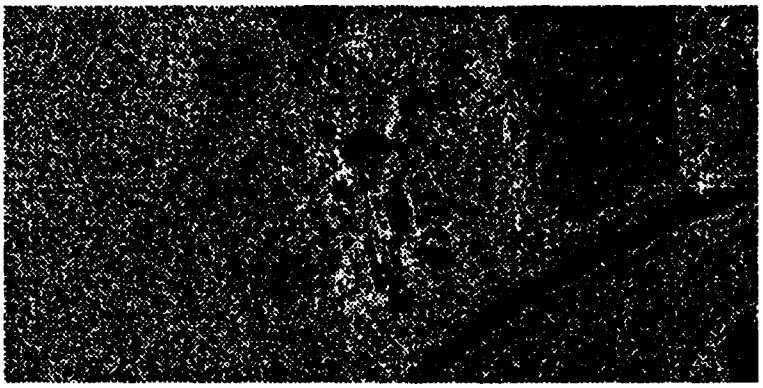

Figure 23. M98F09 HH Polarization 1024 × 512

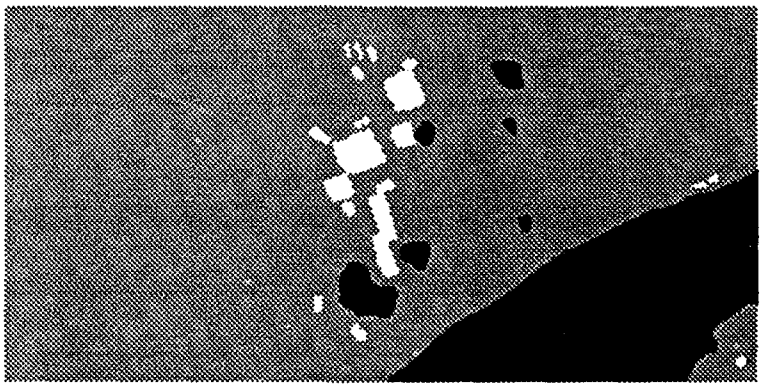

Figure 24. Hand Segmented Template M98F09

4.5.6 **M98F09** This image contains many cultural items. In addition to the long New England style farm house in the center of the image, the image also contains a large barn, a garage, several smaller sheds with farm equipment and vehicles scattered across the image. There is a road, corner reflectors, a pond with a boat, and several fences also present. The region between the road and the pond contains a tree farm with a grassy region surrounding the pond. Even with an aerial photograph the resulting image truth template of this frame is questionable. The aerial photo was not taken at the same time the image was collected thus the location of the vehicles in this image is indeterminate. Figure 24 is the image truth of the this image. Estimated accuracy is low. This image was subjectively evaluated.

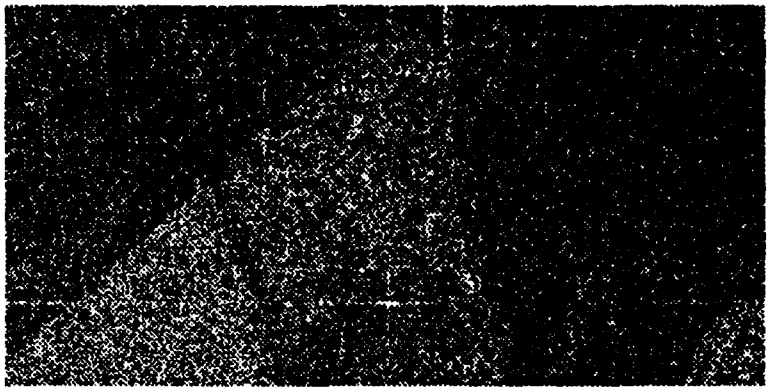

Figure 25. M98F10 HH Polarization 1024 × 512

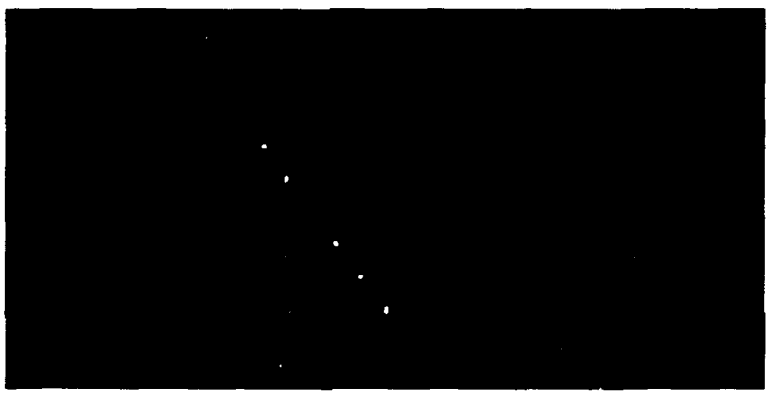

Figure 26. Corner Reflector Template M98F10

4.5.7 **M98F10** This image contains a corner reflector calibration array. In addition to the line of corner reflectors there were also camouflage nets both tented and laying on the ground. Camouflage poles hammered into the ground were also part of the scene. Ground truth data available for this image included photos of all of the individual components but no detailed site drawings were available to place the components in relationship to each other. Ground truth photographs indicated that the area where the calibration array was placed had been mowed. The difference in darkness values in the image is believed to be the boundary between the mowed and unmowed sections of the field. With the exception of the corner reflector placement template (Figure 26) no image truth template of this image was created.

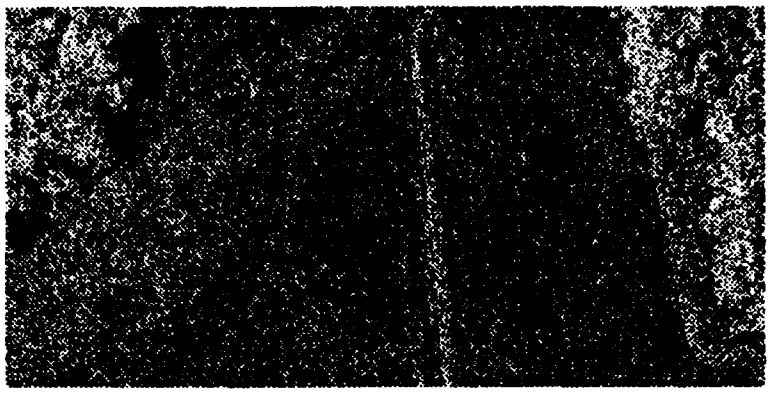

Figure 27. M98F11 HH Polarization 1024 × 512

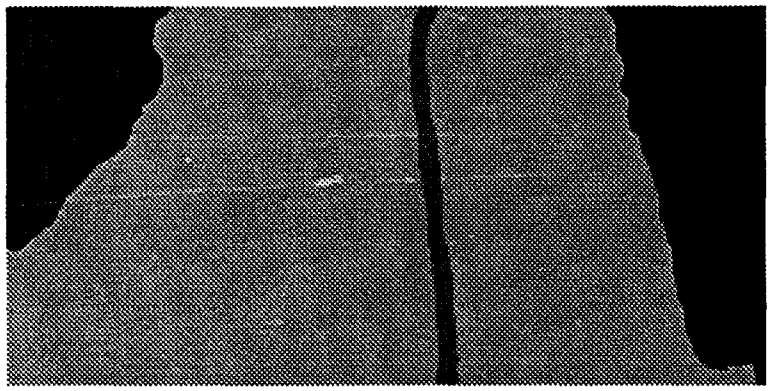

Figure 28. Hand Segmented Template M98F11

4.5.8 **M98F11** This image contains tree, field and road regions. The boundaries between the different regions were reasonably defined. Aerial photography and the radar image indicated a different texture region to the left of the road, near the bottom of the image. Precise ground truth made it impossible to image truth this region. The hand segmented image truth template shown in Figure 28 was used to evaluate this image. Because of this region of uncertainty the accuracy of the resulting image truth is estimated to be 90%.

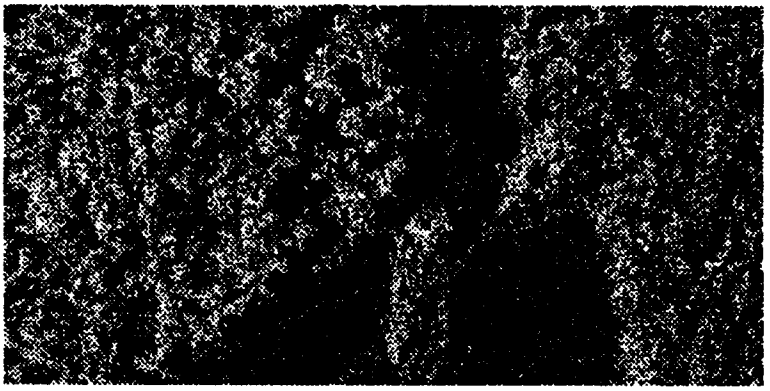

Figure 29. M98F12 HH Polarization 1024 × 512

Figure 30. H ..d Segmented Template M98F12

4.5.9 **M98F12** This image contains only tree and field regions. The boundary between the regions is reasonably defined. Figure 30 is the hand segmented image truth template for this frame. The resulting image truth template is estimated to be 95% accurate.

4.6 Evaluation of Segmentation

After the correlation dimension image for each polarization combination was calculated the images were evaluated to determine the usefulness of correlation dimension estimation for SAR image segmentation. Two separate methods of evaluation were performed depending on the class of data in the imagery. For frames containing only naturally occurring regions a image truth template was constructed using the original SAR image and the limited site information. Threshold sensitivity plots were generated by analytically comparing the image truth templates with segmented correlation dimension images with various thresholds. Images containing cultural items or even natural regions affected by the presence of man (i.e mowed fields) were difficult to accurately image truth without detailed ground truth. Thus, on images containing cultural regions, a subjective evaluation was performed.

4.7 Evaluation Methods

The evaluation of the results of these two different approaches were used to determine the usefulness of performing segmentation on a single correlation dimension image. For frames containing only naturally occurring regions (i.e. trees, fields, and/or shadows) an analytical approach was taken to evaluate the accuracy of the thresholding and median filter approach to segmenting an individual correlation dimension image. In this method, approximately 25 correlation dimension images were created using various thresholds. Each segmented correlation dimension image was compared pixel by pixel to the image truth template with the overall percentage correct and the percent correct for each region present calculated for every threshold. For a particular threshold, the total percent correct, percent correct region 1 and percent correct region 2 were plotted. The result of plotting these points over a range of thresholds was a threshold sensitivity plot. The accuracy of using a particular threshold could be obtained by reading the threshold sensitivity plot. The threshold where the three curves had an equal percentage correct was chosen as the optimum

threshold to use for the separation of the two regions. Picking this threshold resulted in a threshold independent of the distribution of regions within a scene.

Figure 31 is an example of a plot resulting from the method described above. The correlation dimension image used to generate the data for this plot was calculated using M98F11 all polarizations. At correlation dimension value 1.982 both tree and field regions were 90% correct as compared to the template.

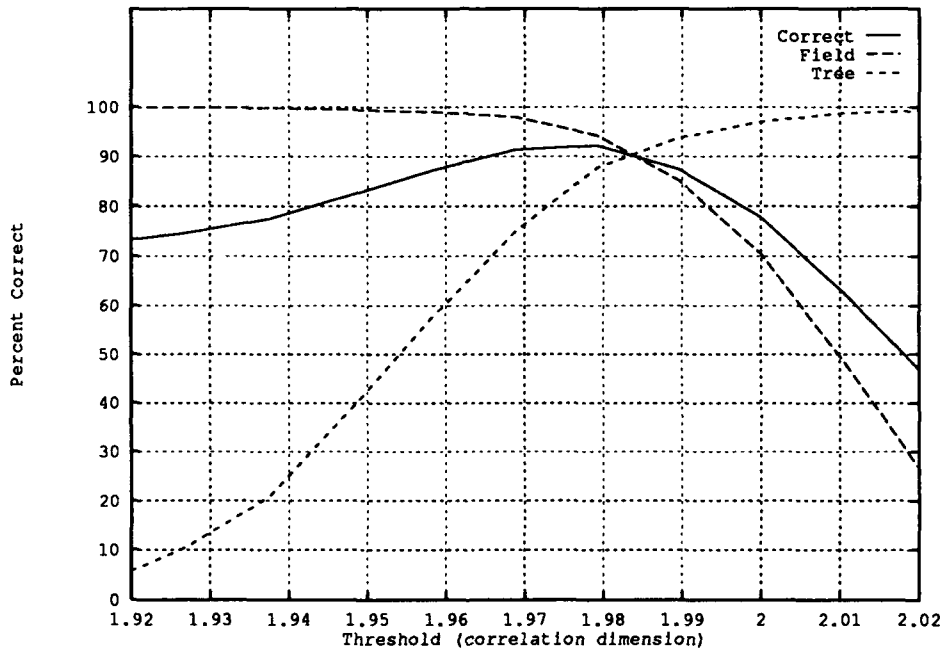

Figure 31. Threshold Sensitivity Plot M98F11 All Polarizations WS 16 × 16

For frames containing cultural items, a subjective evaluation on the accuracy of the correlation dimension approach will be presented.

The following images: M85F27, M85F28, M98F07, M98F08, M98F11 and M98F12 will be analytically evaluated. The remainder of the images: M85F30, M98F09 and M98F10 will be subjectively evaluated.

4.8 Analytical Evaluation

In this section the results of the analytical approach will be presented. Of the six frames chosen to be used for this evaluation method, only two of those contained large regions of shadows. Thus, all six frames will be used to determine the tree–field threshold and corresponding accuracy and only two frames, M85F27 and M85F28, will be used to determine the field–shadow threshold and corresponding accuracy.

4.8.1 Tree–Field Boundary Analysis

4.8.1.1 **Window Size 16×16** Shown in Table 2 are percentages of the analytical tree-field evaluations of the six frames for all combinations of polarizations where the window size for estimating the correlation dimension was 16×16. The table shows that the overall accuracy across all six images was 85.9%. Table 2 also shows the mean and standard deviations across polarizations and across images. Overall, the correlation dimension images generated using all four combinations of polarizations had a higher percentage correct than any other combination of polarizations. Intuitively this makes sense, the more data available the more accurate the representation. However, this intuitive approach doesn't hold up over all the possible combinations of polarizations. Looking at the combined mean of all six images, HH and VV polarizations do not contain more information than the four combinations of three polarizations each, but HH and VV each have a higher percentage correct. That statement is not true for each individual image. With the exception of one image M98F07, the correlation dimension image calculated using a combination of all four polarizations produces more accurate results than any other combination. In M98F07, the VV polarization had the highest percentage correct. Another result that holds overall, but not over every specific image, is that the combinations of polarizations containing one cross polarization (i.e. VH or HV) or two cross polarizations together (with the exception of all four polarizations) are the combinations that are below the mean of all combinations.

Table 2. Tree-Field Percentage Correct (Equal Percentage Correct Point) Window Size 16 × 16

Tree-Field	Mission 85		Mission 98				Combined	
WS 16 × 16	Frame		Frame				Statistics	
Polarization	27	28	07	08	11	12	Mean	Stdev
All	83	96	97	90	90	93	91.5	4.646
HH	82	90	96	84	90	90	88.7	4.570
HV	59	82	93	89	87	85	82.5	10.416
VH	62	78	89	85	89	85	81.3	9.393
VV	83	90	98	86	89	83	88.2	5.145
HH, HV	77	91	96	87	90	90	88.5	5.795
HH, VH	77	90	97	88	88	88	88.0	5.860
HH, VV	80	93	96	87	88	91	89.2	5.080
HV, VH	61	83	91	83	80	85	80.5	9.341
HV, VV	77	92	92	88	89	86	87.3	5.088
VH, VV	77	88	96	89	89	88	87.8	5.580
HH, HV, VH	63	81	82	80	80	80	79.3	8.479
HH, HV, VV	77	89	90	86	89	93	87.3	5.055
HH, VH, VV	77	92	91	89	88	91	88.0	5.099
HV, VH, VV	69	83	91	80	81	78	80.3	6.524
Mean	73.6	87.9	93.7	86.1	87.0	86.9	85.9	—
Stdev	8.155	5.018	2.891	3.043	3.464	4.4434	—	—

The percentage correct for each frame also corresponds to the subjective evaluation of the accuracy of the image truth template used to evaluate the frame. The frames where the templates were thought to be accurate are also the ones that have the higher percentages correct. It is believed that higher percentages could be obtained with this correlation dimension estimation method if more accurate image truth templates were available. Without detailed ground truth information an accurate evaluation of this method is not possible. Even though some error has been introduced because the image truth templates are not totally accurate, the results obtained (i.e. optimum combinations of polarizations, window sizes) should not be affected greatly.

If M85F27, the image containing the lowest overall percentages correct, was removed from the combined statistics, the values shown in Table 3 result.

The overall percentage correct increases to 88.5% and the standard deviations are all 5.036% or less. When M85F27 was included the standard deviations varied up to as much as 10.416%.

From the above results, it appears that the correlation dimension estimate is a valid feature to use to segment between tree and field regions within a SAR image.

Shown in Table 4 are correlation dimension thresholds corresponding to the percentages correct data from Table 2. Examining Table 4 reveals that the thresholds for a window size of 16 $\times$ 16 hold for a specific combination of polarizations over all of the images analyzed. Although one correlation dimension threshold does not hold over all possible combinations of polarizations, one correlation dimension threshold can be used over any specific polarization combination. For example, using the mean threshold from correlation dimension images calculated using all polarizations combined, 1.9768, will produce a good segmentation between tree and field regions regardless of the frame used if the the correlation dimension image used was calculated using all polarizations.

Table 3. Tree-Field Percentage Correct(Equal Percentage Correct Point) Window Size 16 × 16 (M85F27 not included)

Tree-Field	Mission 85	Mission 98				Combined	
WS 16 × 16	Frame	Frame				Statistics	
Polarization	28	07	08	11	12	Mean	Stdev
All	96	97	90	90	93	93.2	2.926
HH	90	96	84	90	90	92.4	2.939
HV	82	93	89	87	85	87.2	3.709
VH	78	89	85	89	85	85.2	4.020
VV	90	98	86	89	83	89.2	5.036
HH, HV	91	96	87	90	90	90.8	2.956
HH, VH	90	97	88	88	88	90.2	3.487
HH, VV	93	96	87	88	91	91.0	3.286
HV, VH	83	91	83	80	85	84.4	3.666
HV, VV	92	92	88	89	86	89.4	2.332
VH, VV	88	96	89	89	88	90.0	3.033
HH, HV, VH	81	82	80	80	80	82.6	4.716
HH, HV, VV	89	90	86	89	93	89.4	2.245
HH, VH, VV	92	91	89	88	91	90.2	1.470
HV, VH, VV	83	91	80	81	78	82.6	4.499
Mean	87.9	93.7	86.1	87.0	86.9	88.5	—
Stdev	5.018	2.891	3.043	3.464	4.4434	—	—

Table 4. Tree-Field Correlation Dimension Thresholds(Equal Percentage Correct Point) Window Size 16 × 16

Tree-Field	Mission 85		Mission 98				Combined	
WS 16 × 16	Frame		Frame				Statistics	
Polarization	27	28	07	08	11	12	Mean	Stdev
All	1.989	1.974	1.962	1.982	1.982	1.972	1.9768	.00869
HH	1.826	1.806	1.806	1.829	1.823	1.814	1.8173	.009232
HV	1.848	1.842	1.820	1.831	1.826	1.826	1.8321	.009771
VH	1.844	1.837	1.820	1.831	1.826	1.827	1.8308	.007820
VV	1.827	1.810	1.812	1.828	1.812	1.809	1.8163	.007972
HH, HV	1.974	1.960	1.938	1.962	1.952	1.951	1.9562	.011112
HH, VH	1.969	1.959	1.942	1.967	1.958	1.946	1.9568	.009957
HH, VV	1.898	1.885	1.884	1.908	1.912	1.892	1.8965	.010673
HV, VH	1.889	1.889	1.868	1.854	1.869	1.846	1.8692	.018673
HV, VV	1.978	1.963	1.933	1.960	1.947	1.942	1.9538	.014871
VH, VV	1.973	1.959	1.937	1.962	1.948	1.942	1.9535	.012366
HH, HV, VH	1.979	1.971	1.950	1.960	1.957	1.947	1.9607	.011235
HH, HV, VV	1.993	1.983	1.961	1.993	1.996	1.983	1.9848	.011782
HH, VH, VV	1.991	1.980	1.965	1.996	1.993	1.982	1.9845	.010436
HV, VH, VV	1.982	1.974	1.950	1.960	1.951	1.944	1.9602	.013643

Table 5. Tree-Field Percentage Correct (Equal Percentage Correct Point) Window Size 8×8

Tree-Field	Mission 85		Mission 98				Combined	
WS 8×8	Frame		Frame				Statistics	
Polarization	27	28	07	08	11	12	Mean	Stdev
All	63	73	96	86	88	90	82.7	11.190
HH	55	67	82	70	78	77	71.5	8.921
HV	58	63	69	68	66	66	65.0	3.652
VH	57	60	70	66	63	67	63.8	4.375
VV	55	61	80	72	80	80	71.3	9.994
HH, HV	59	63	82	78	81	81	74.0	9.345
HH, VH	59	71	82	79	80	81	75.3	8.138
HH, VV	64	73	88	81	86	92	80.7	9.551
HV, VH	62	65	91	73	70	72	72.2	9.263
HV, VV	60	62	81	79	79	78	73.2	8.668
VH, VV	60	66	82	80	79	78	74.2	8.174
HH, HV, VH	63	70	93	80	81	80	77.8	9.406
HH, HV, VV	64	72	88	87	87	91	81.5	9.912
HH, VH, VV	62	69	92	87	87	92	81.5	11.673
HV, VH, VV	60	70	92	79	78	78	76.2	9.703
Mean	60.1	67.0	84.5	77.7	78.9	80.2	74.7	—
Stdev	2.863	4.336	7.710	6.394	7.191	8.002	—	—

4.8.1.2 **Window Size 8×8** Shown in Table 5 are percentages of the 8×8 window size tree-field analytical evaluation over the six frames for all combinations of polarizations. The overall results over the six frames is a mean percent correct of 74.7%. As in the 16×16 case the correlation dimension image calculated using all polarizations resulted in the highest percentages correct. The combination of all polarizations does not have the highest percentage correct for each individual frame but it does for all frames combined. The percentages correct for 8×8 are lower than the percent correct for a window size of 16×16. There are two possible explanations for this result.

The first possible explanation is that, since the correlation dimension estimation method is a statistical method, reducing the window size from 16×16 or 256

pixels to 8×8 or 64 pixels does not provide a large enough sample of pixels to be statistically valid. The second possible explanation is that, since the resulting resolution for the smaller window size is finer, the image truth template must be more accurate to evaluate the segmentation. Since the same image truth is used for both window sizes the image truth could be causing lower percentages to occur. The image truth template is not accurate enough to identify every 8×8 region correctly. Both explanations given above contribute to the lower percentages correct. Shown in Table 6 are the thresholds corresponding to the percentages shown in Table 5. As in the case of the 16×16 window size, the thresholds are consistent for the same combinations of polarizations over all six images. The standard deviations for the 8×8 window size are lower than the standard deviations for the 16×16 window size indicating that the thresholds seem to hold tighter over all the images for a specific combination of polarization.

4.8.2 **Field-Shadow Boundary Analysis** Shown in Table 7 are the results of the analytical analysis for the Field-Shadow threshold evaluation. Results from both 8×8 and 16×16 window sizes are shown. The overall result, the 16×16 window size had a 87.6% correct versus the 8×8 window size having a 73.3% correct. As in the tree-field threshold evaluation the 8×8 window size had over a 10% lower overall percentage correct value.

Table 8 contains the thresholds corresponding to the percentages given in Table 7. As before, the thresholds hold over the same combination of polarizations.

4.8.3 **Optimum Median Filter Selection** The median filter used after thresholding the correlation dimension image was 5×5 for all of the results presented thus far for both window sizes, 16×16 and 8×8. As the window sizes decreased from 16×16 to 8×8 the question arose as to whether the size of the median filter should decrease from 5×5 to 3×3. Table 9 contains the results of a comparison of images generated using a 3×3 and a 5×5 median filter to the image truth template.

Table 6. Tree-Field Correlation Dimension Thresholds(Equal Percentages Correct Point) Window Size 8×8

Tree-Field	Mission 85		Mission 98				Combined	
WS 8×8	Frame		Frame				Statistics	
Polarization	27	28	07	08	11	12	Mean	Stdev
All	2.045	2.026	2.026	2.030	2.032	2.022	2.0302	.007360
HH	1.890	1.881	1.884	1.889	1.887	1.887	1.8863	.003037
HV	1.901	1.895	1.888	1.890	1.889	1.890	1.8922	.004525
VH	1.900	1.893	1.888	1.890	1.890	1.890	1.8918	.003933
VV	1.890	1.882	1.884	1.888	1.886	1.886	1.8860	.002582
HH, HV	2.002	1.992	1.982	1.992	1.986	1.988	1.9903	.006263
HH, VH	1.999	1.992	1.981	1.992	1.987	1.988	1.9890	.005520
HH, VV	1.936	1.922	1.926	1.945	1.952	1.939	1.9367	.010323
HV, VH	1.920	1.910	1.907	1.896	1.901	1.896	1.9050	.008485
HV, VV	2.002	1.992	1.981	1.990	1.985	1.986	1.9893	.006675
VH, VV	2.002	1.991	1.982	1.990	1.986	1.986	1.9895	.006318
HH, HV, VH	1.998	1.983	1.982	1.976	1.979	1.973	1.9818	.007988
HH, HV, VV	2.021	2.006	1 998	2.021	2.026	2.014	2.0143	.009672
HH, VH, VV	2.02	2.001	2.001	2.022	2.026	2.016	2.0143	.009877
HV, VH, VV	1.999	1.982	1.979	1.976	1.978	1.971	1.9808	.008783

Table 7. Field-Shadow Percentage Correct (Equal Percentage Correct Point)

Window Size	8 × 8				16 × 16			
Field-Shadow	Frame		Statistics		Frame		Statistics	
Polarization	27	28	Mean	Stdev	27	28	Mean	Stdev
All	80	71	75.5	.045	93	91	92.0	1.0
HH	59	65	62.0	.030	76	85	80.5	4.5
HV	71	75	73.0	.020	90	92	91.0	1.0
VH	68	74	71.0	.030	88	92	90.0	2.0
VV	59	64	61.5	.025	72	84	78.0	6.0
HH, HV	70	70	70.0	0.0	83	90	86.5	3.5
HH, VH	70	76	73.0	.030	80	88	84.0	4.0
HH, VV	70	71	70.5	.005	80	86	83.0	3.0
HV, VH	88	88	88.0	0.00	94	94	94.0	0.0
HV, VV	73	73	73.0	0.00	82	90	86.0	4.0
VH, VV	71	68	69.5	.015	82	88	85.0	3.0
HH, HV, VH	83	82	82.5	.005	91	92	91.5	0.5
HH, HV, VV	75	71	73.0	.020	90	91	90.5	0.5
HH, VH, VV	76	72	74.0	.020	88	90	89.0	1.0
HV, VH, VV	85	81	83.0	.020	92	93	92.5	0.5
Mean	73.2	73.4	73.3	—	85.4	89.7	87.6	—
Stdev	8.1	6.2	—	—	6.4	2.9	—	—

Table 8. Field-Shadow Correlation Dimension Thresholds(Equal Percentage Correct Point)

Window Size	8×8				16×16			
Field-Shadow	Frame		Statistics		Frame		Statistics	
Polarization	27	28	Mean	Stdev	27	28	Mean	Stdev
All	2.057	2.028	2.0425	.0145	2.020	2.002	2.0110	.0090
HH	1.890	1.881	1.8855	.0045	1.848	1.813	1.8305	.0175
HV	1.903	1.898	1.9005	.0025	1.862	1.851	1.8565	.0055
VH	1.902	1.896	1.8990	.0030	1.857	1.847	1.8520	.0050
VV	1.890	1.883	1.8865	.0035	1.837	1.819	1.8280	.0090
HH, HV	2.005	1.995	2.0000	.0050	1.993	1.972	1.9825	.0105
HH, VH	2.003	1.996	1.9995	.0035	1.984	1.972	1.9780	.0060
HH, VV	1.940	1.922	1.9310	.0090	1.928	1.898	1.9130	.0150
HV, VH	1.928	1.919	1.9235	.0045	1.911	1.903	1.9070	.0040
HV, VV	2.006	1.996	2.0010	.0050	1.994	1.978	1.9860	.0080
VH, VV	2.006	1.993	1.9995	.0065	1.990	1.969	1.9795	.0105
HH, HV, VH	2.008	1.988	1.9980	.0100	2.003	1.988	1.9955	.0075
HH, HV, VV	2.028	2.007	2.0175	.0105	2.020	2.002	2.0110	.0090
HH, VH, VV	2.026	2.005	2.0155	.0105	2.013	2.001	2.0070	.0060
HV, VH, VV	2.008	1.988	1.9980	.0100	2.008	1.992	2.0000	.0080

Table 9. Comparison Between 3 × 3 and 5 × 5 Median Filter Operation Using MSN 98 Frame 07

MSN 98 F07	Tree-Field	
WS 8 × 8	Median Filter	
Polarization	3 × 3	5 × 5
All	90	96
HH	72	82
HV	65	69
VH	65	70
VV	71	80
HH, HV	75	82
HH, VH	75	82
HH, VV	80	88
HV, VH	85	91
HV, VV	72	81
VH, VV	72	82
HH, HV, VH	88	93
HH, HV, VV	82	88
HH, VH, VV	85	92
HV, VH, VV	86	92

M85F07 was used for the comparison because it had the highest percentages correct of all the frames. As can be observed from Table 9 using a 5×5 median filter provides higher percentages correct.

4.8.4 **Imagery Resulting From Analytical Evaluations** The next six pages contain the segmented images resulting for the thresholds chosen during the above analytical evaluation. The images shown were created using all polarizations. First the SAR image is presented followed by the correlation dimension image calculated with a 16×16 window size and then the correlation dimension image caculated with a 8×8 window size.

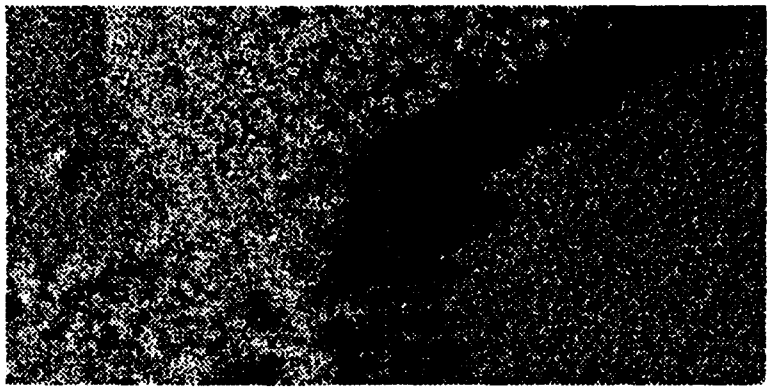

Figure 32. M85F27 HH Polarization 1024 × 512

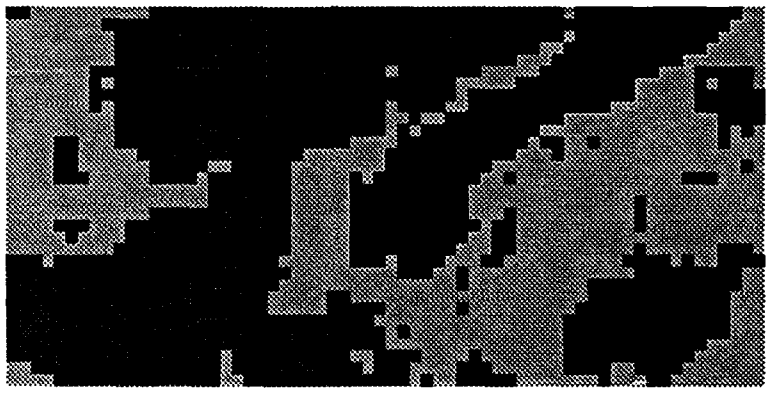

Figure 33. Segmented M85F27 Tree-Field-Shadow All Polarizations WS 16 × 16

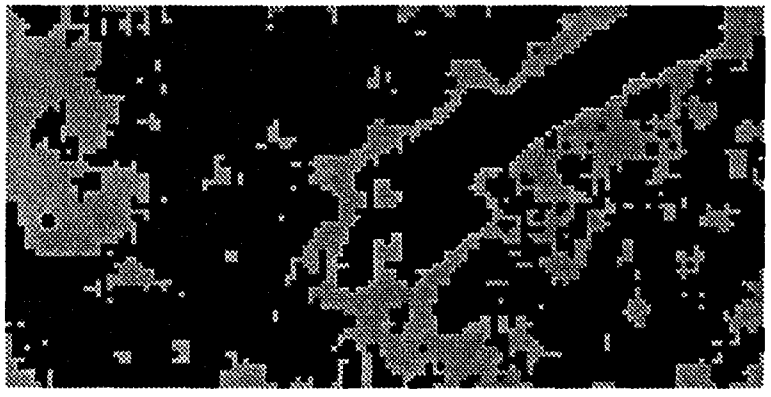

Figure 34. Segmented M85F27 Tree-Field-Shadow All Polarizations WS 8 × 8

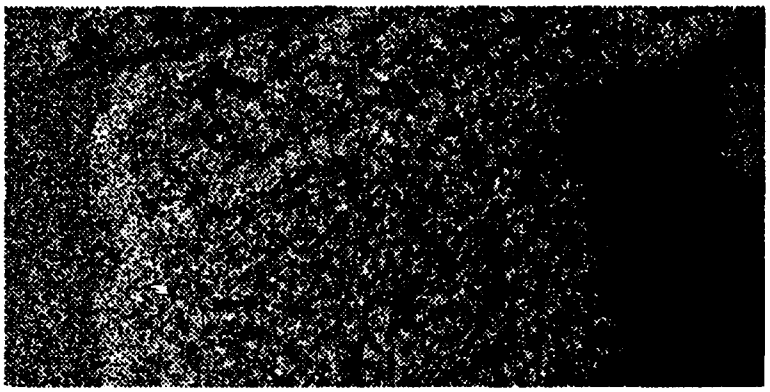

Figure 35. M85F28 HH Polarization 1024 × 512

Figure 36. Segmented M85F28 Tree-Field-Shadow All Polarizations WS 16 × 16

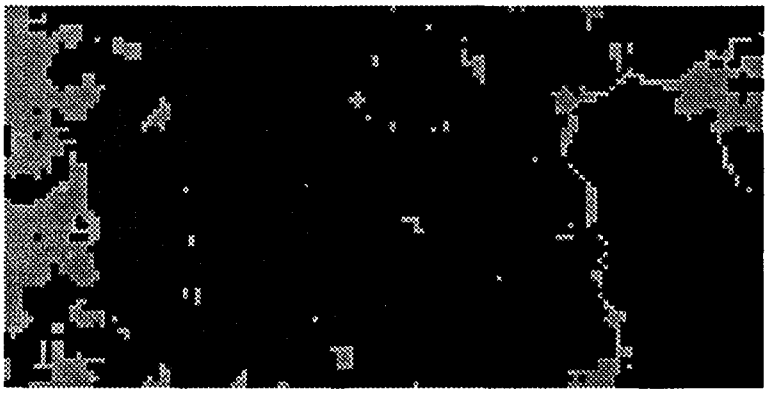

Figure 37. Segmented M85F28 Tree-Field-Shadow All Polarizations WS 8 × 8

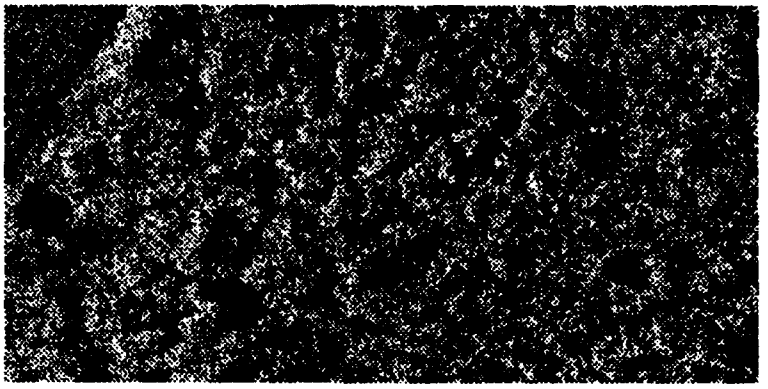

Figure 38. M98F07 HH Polarization 1024 × 512

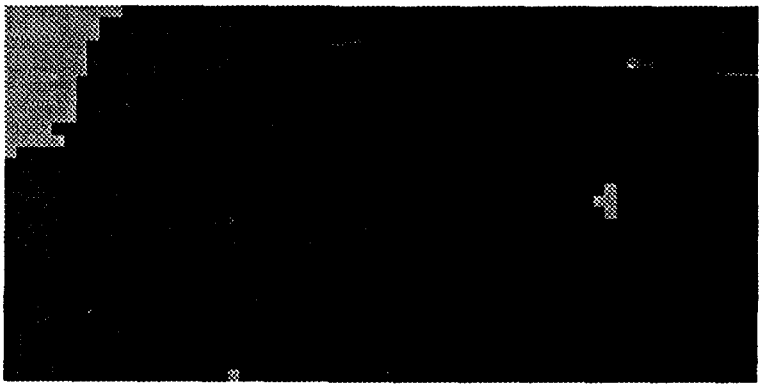

Figure 39. Segmented M98F07 Tree-Field All Polarizations Window Size 16 × 16

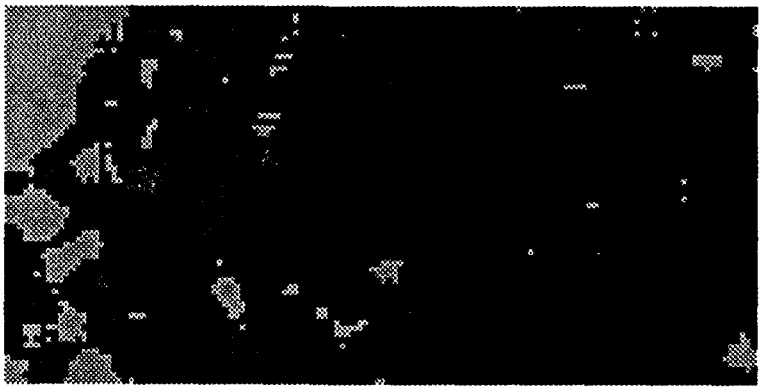

Figure 40. Segmented M98F07 Tree-Field All Polarizations Window Size 8 × 8

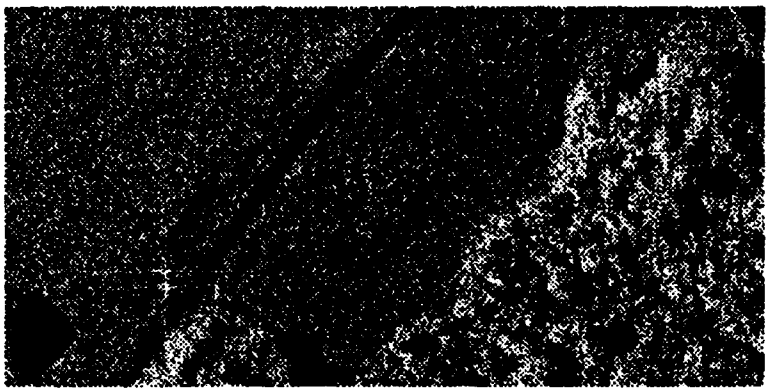

Figure 41. M98F08 HH Polarization 1024 × 512

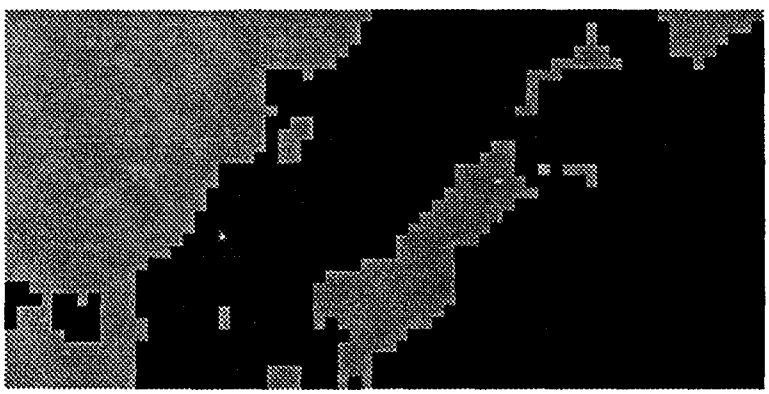

Figure 42. Segmented M98F08 Tree-Field All Polarizations Window Size 16 × 16

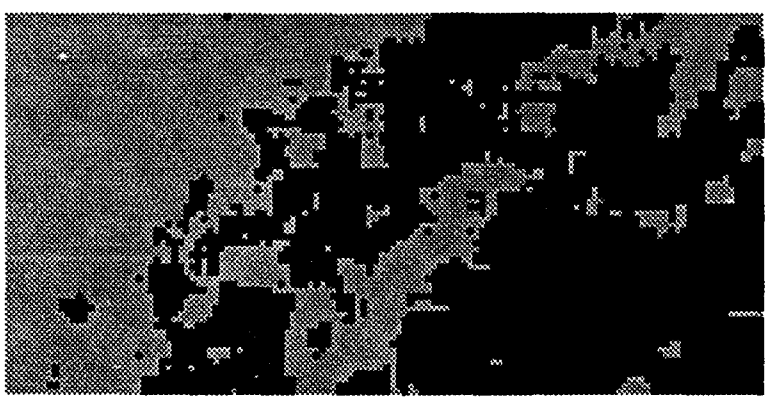

Figure 43. Segmented M98F08 Tree-Field All Polarizations Window Size 8 × 8

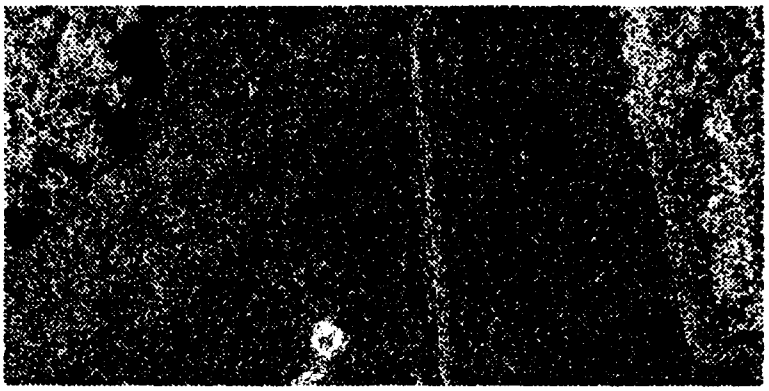

Figure 44. M98F11 HH Polarization 1024 × 512

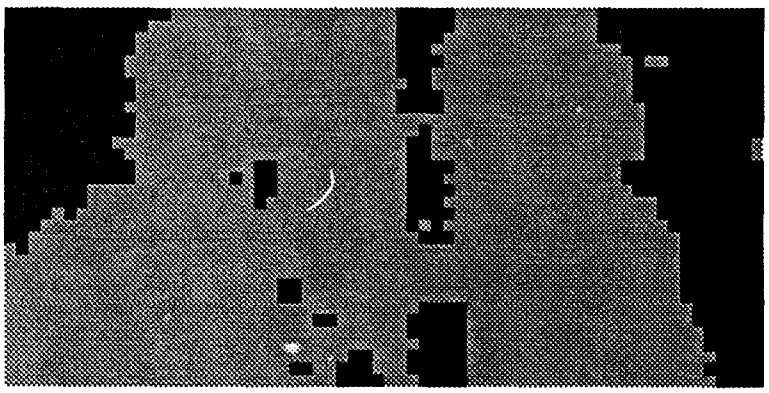

Figure 45. Segmented M98F11 Tree-Field All Polarizations Window Size 16 × 16

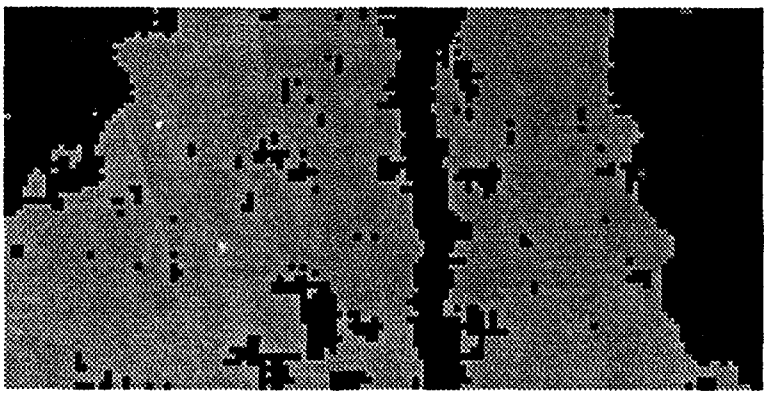

Figure 46. Segmented M98F11 Tree-Field All Polarizations Window Size 8 × 8

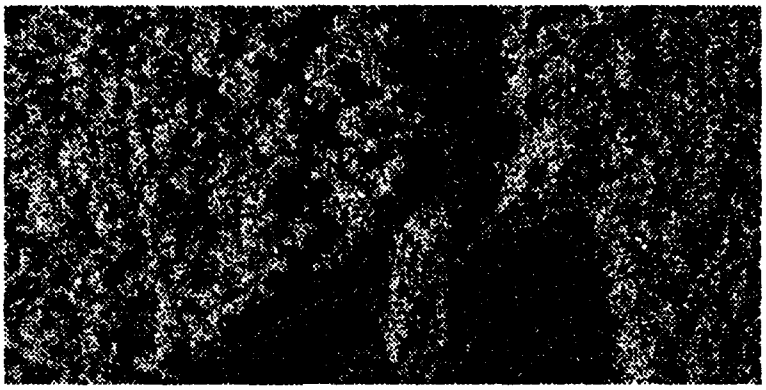

Figure 47. M98F12 HH Polarization 1024 × 512

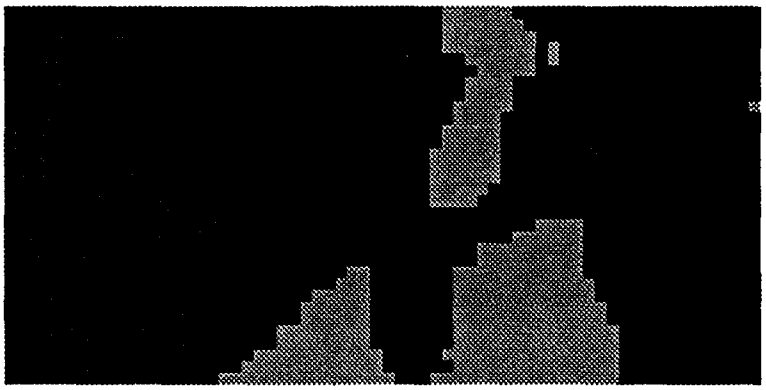

Figure 48. Segmented M98F12 Tree-Field All Polarizations Window Size 16 × 16

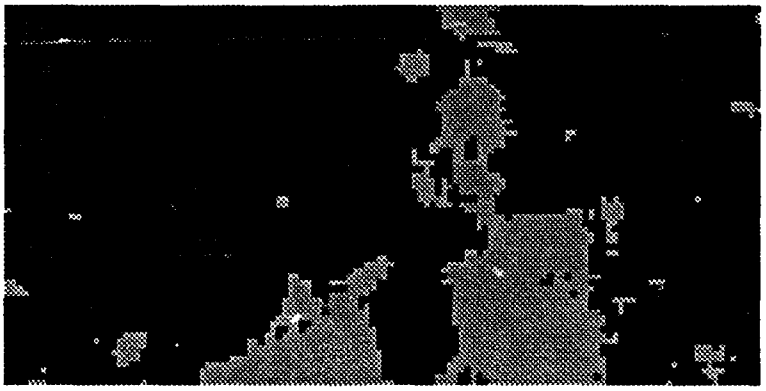

Figure 49. Segmented M98F12 Tree-Field All Polarizations Window Size 8 × 8

As can be observed from the preceding figures, correlation dimension estimates show potential as a feature for segmenting between naturally occurring regions.

4.9 Subjective Evaluation

The difficulty encountered when trying to create a 64×32 or 128×64 image truth template from a 1024×512 radar imagery without proper ground truth documentation has already been discussed. Due to this inability to produce an accurate 64×32 or 128×64 image truth template for SAR imagery containing cultural items no analytical evaluation of cultural frames was performed. The analytical method used to evaluate the scenes in the previous section was performed on a pixel by pixel basis. Because the image truth templates for cultural data has pixels that are off by one pixel, a pixel by pixel evaluation results in a very low percentage correct. However, when comparing the correlation dimension image and the image truth template, a close relationship between where the cultural items appear in the correlation dimension image and where they appear on the image truth template can be observed.

The limited amount of SAR imagery containing cultural items processed during this thesis effort suggest that correlation dimension estimates of cultural regions/objects is low compared to naturally occurring regions. Histograms of the correlation dimension estimates of frames containing cultural items are shown in Figures 50 - 52. These correlation dimension estimates were calculated using all polarizations and a 16×16 window size. The points on the lower side of the histogram correspond to objects in the SAR image that are man–made. All of the imagery processed containing cultural objects indicated the same phenomena. Cultural objects possess lower correlation dimension estimates than natural objects.

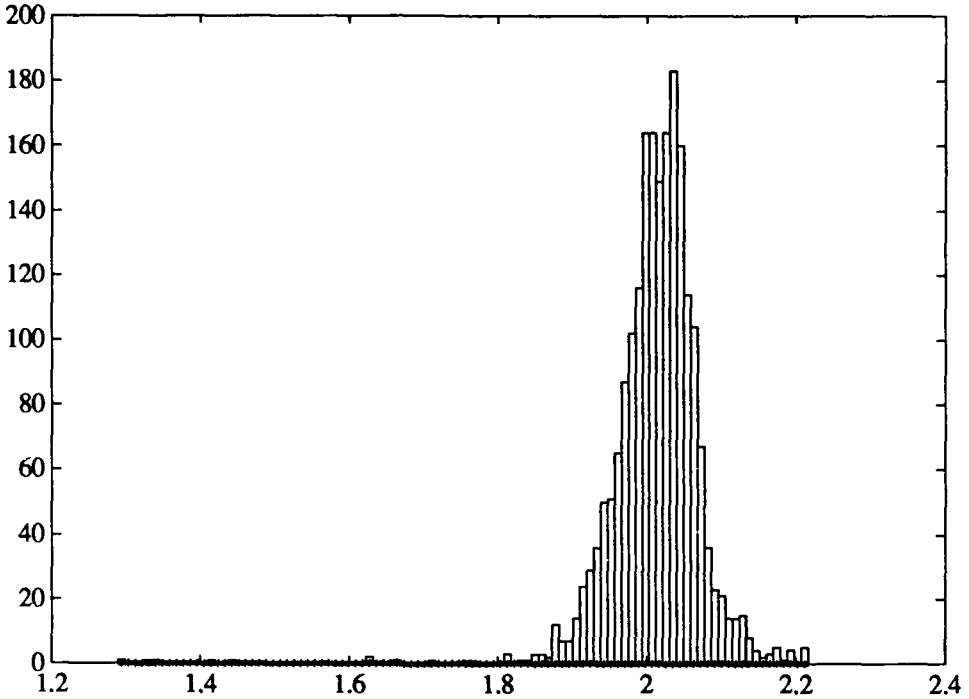

Figure 50. Histogram of M85F30 All Polarizations 16 × 16

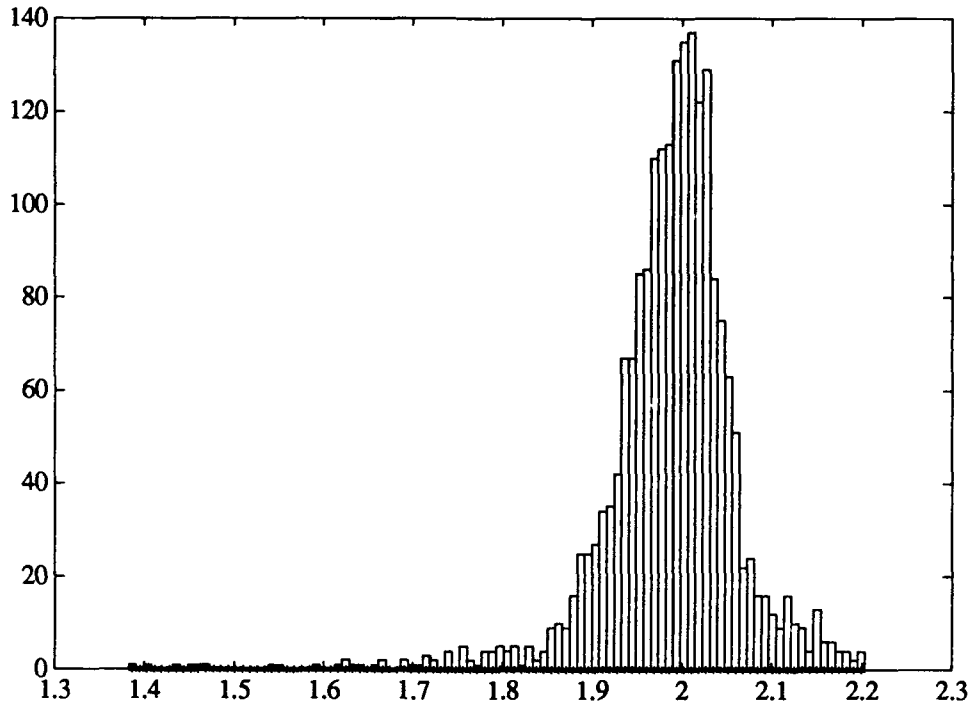

Figure 51. Histogram of M98F09 All Polarizations 16 × 16

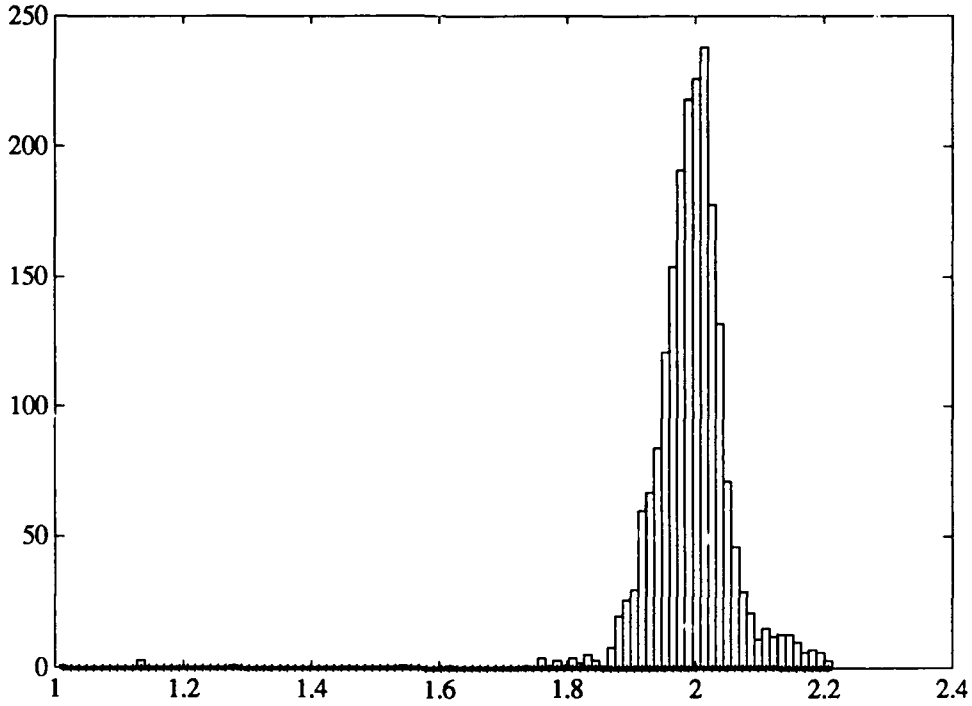

Figure 52. Histogram of M98F10 All Polarizations 16 × 16

Thresholding of the correlation dimension image yielded the location of the cultural objects. Even though a pixel by pixel analytical evaluation yielded a low percentage correct, looking at the thresholded correlation dimension image indicated the thresholding of correlation dimension could locate cultural objects.

Three frames (M85F30, M98F09, M98F10) were subjectively evaluated. In this section the results of the subjective evaluation will be presented.

4.9.1 **M85F30 Subjective Evaluation** Shown in Figure 53 is the HH polarization image of M85F30. A corner reflector array consisting of eight corner reflectors is present in the frame. Figure 54 is the correlation dimension image corresponding of this frame calculated using all polarizations and a window size of 16×16. The correlation dimension values were multiplied by 96 in order to display them as grayscale values midscale between 0 and 255. From this image it can be noted that the lowest values correspond to the location of cultural objects (i.e. corner reflectors) in the image. Figure 55 is the corresponding image truth template for this frame. Shown in Figure 56 is the corner reflector image truth template for this frame. Figure 57 shows the result of thresholding the correlation dimension image. As can be observed from the image all eight corner reflectors and the metal pole near the bottom center of the image was detected. What is actually present at the location on the right hand edge of the image is unknown. Based on correlation dimension estimation, it is cultural. The ground truth was not available to verify this. The segmented image shown in Figure 58 resulted from setting the threshold to the tree–field separation threshold and then performing a median filter operation. The treeline is present in this image. Also note that the area around where the corner reflectors were placed has a lower correlation dimension than the surrounding field. Possibly the traffic in and around the corner reflectors trampled the grass in the field down resulting in a *smoother* surface.

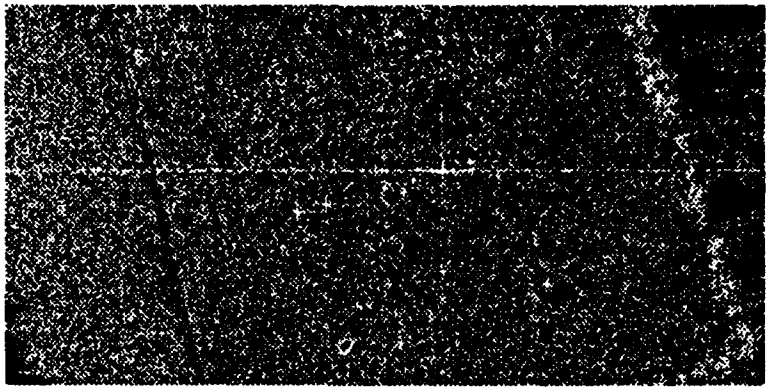

Figure 53. M85F30 HH Polarization 1024 × 512

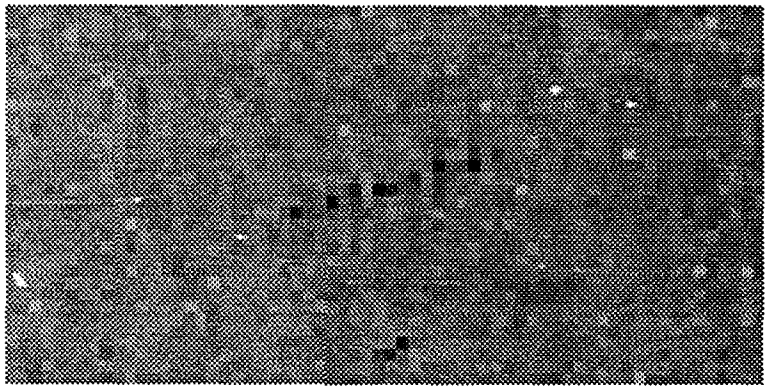

Figure 54. M85F30 Correlation Dimension Values ×96 All Polarizations WS 16×16

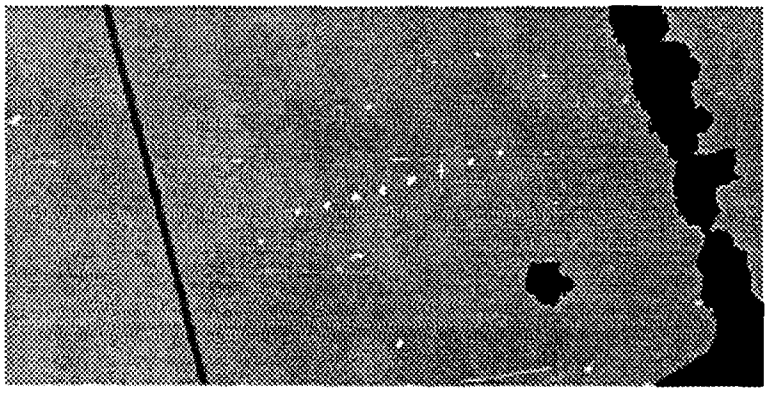

Figure 55. M85F30 Hand Segmented Template 1024 × 512

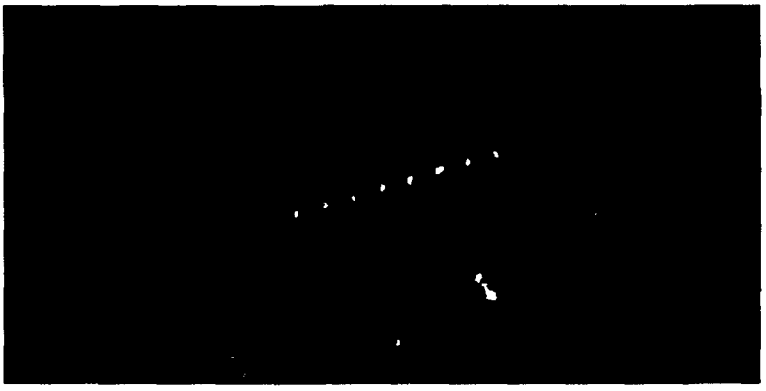

Figure 56. M85F30 Corner Reflector Template 1024 × 512

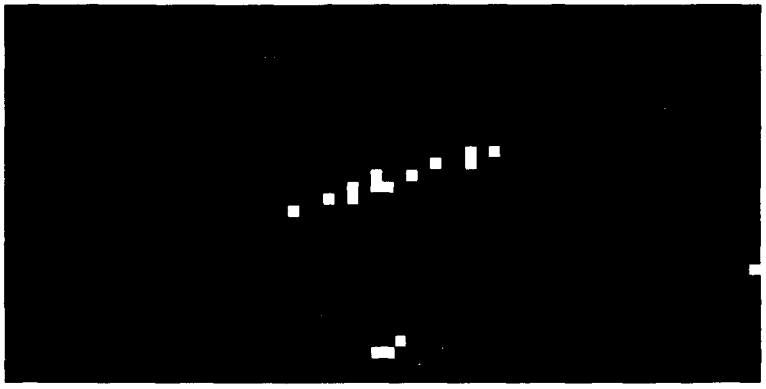

Figure 57. Segmented M85F30 Culture All Polarizations WS 16 × 16

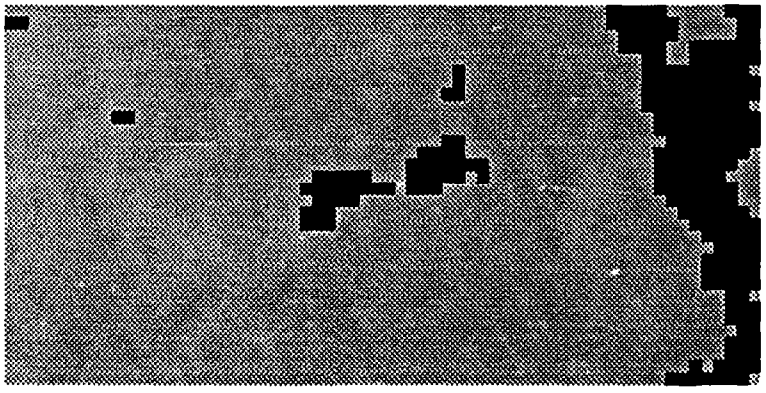

Figure 58. Segmented M85F30 Culture/Trees All Polarizations WS 16 × 16

4.9.2 **M98F09 Subjective Evaluation** Figures 59, 60, and 61 correspond to the original HH polarization SAR, the correlation dimension image and the hand segmented template for M98F09. Observe from Figure 60 that the lower correlation dimension estimates correspond to the location of cultural objects within the scene. Present in the scene are buildings, vehicles, corner reflectors and either a boat or dock on the pond. Figure 62 is the result of reducing the original 1024×512 hand segmented template for M98F09 by 25% twice. Note that the resizing procedure while it results in a template of the proper size (16:1 reduction in size) details of the original image truth template are lost. Shown in Figure 63 is the result of thresholding the correlation dimension image to separate the cultural items. The location of cultural objects indicated in Figure 63 correspond closely to the location of cultural items in the image truth template. Figure 64 is an example of setting the threshold higher then the threshold where cultural objects are completely separable from the rest of the image and then performing a median filter operation. Again the indicated areas correspond closely to the image truth template. Figure 65 is a 128×64 image truth template that was resized from the original image truth template. This template corresponds to a 8:1 reduction in size from the original. Shown in Figure 66 is the thresholded correlation dimension image calculated with window size 8×8 using all polarizations. The light pixels correspond to areas of cultural concentration. The segmented image shown in Figure 67 was generated using a HH polarization correlation dimension image with window size 8×8. The threshold chosen was higher than the value where cultural objects were completely separable. After the threshold was set a median filter operation was performed.

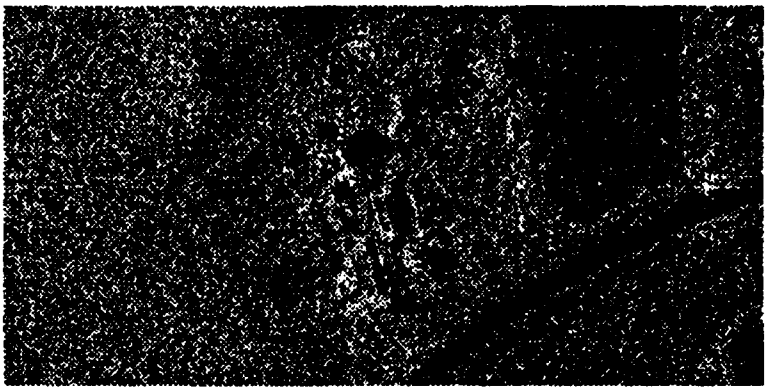

Figure 59. M98F09 HH Polarization 1024 × 512

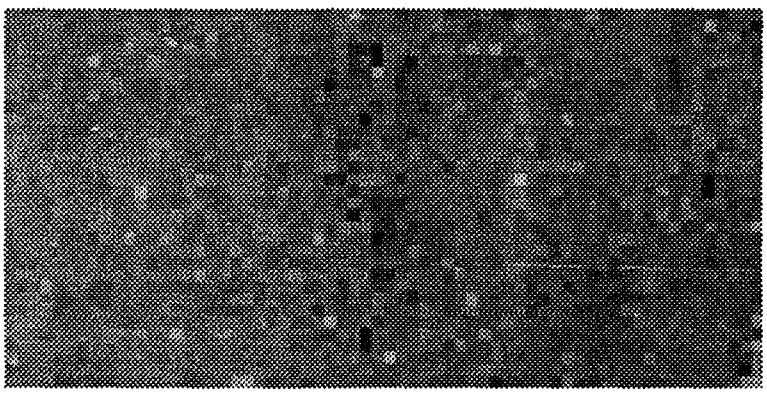

Figure 60. M98F09 Correlation Dimension Values ×96 All Polarizations WS 16×16

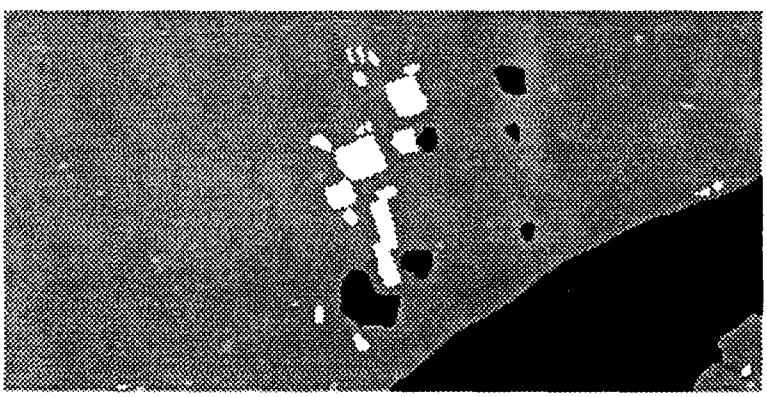

Figure 61. M98F09 Hand Segmented Template 1024 × 512

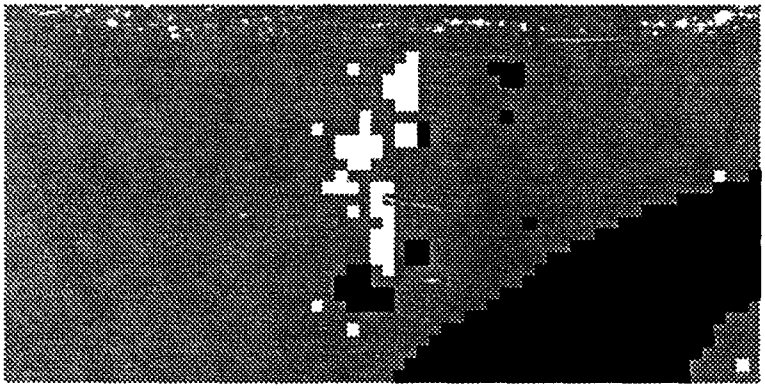

Figure 62. M98F09 Hand Segmented Template 64 × 32

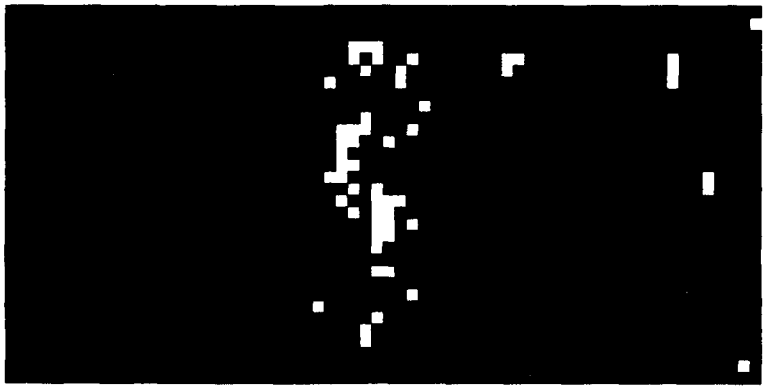

Figure 63. Segmented M98F09 Culture All Polarizations WS 16 × 16

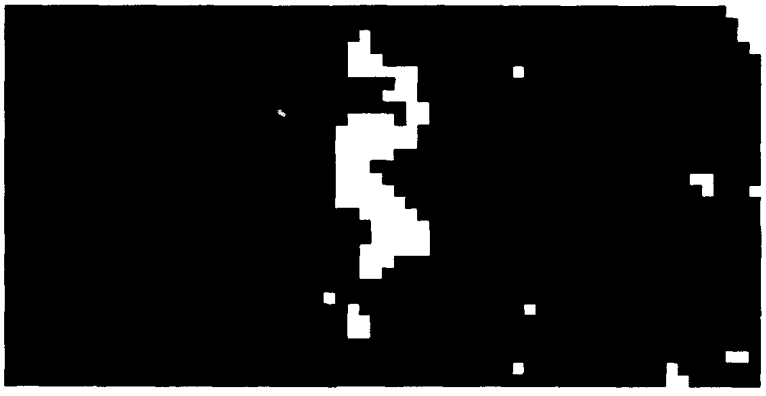

Figure 64. Segmented M98F09 Culture Median Filtered All Polarizations WS 16 × 16

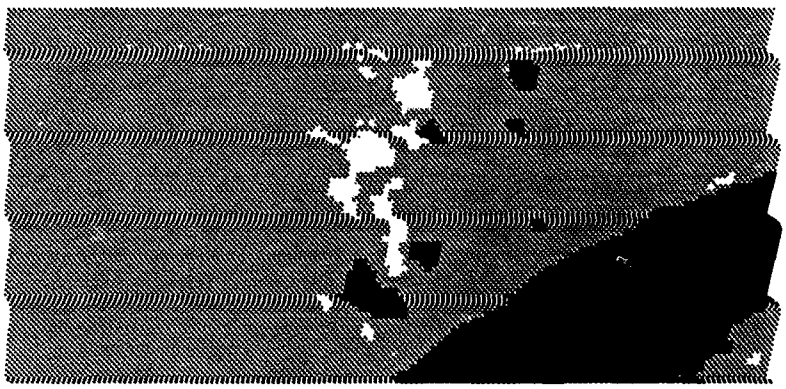

Figure 65. *M98F09 Hand Segmented Template 128 × 64*

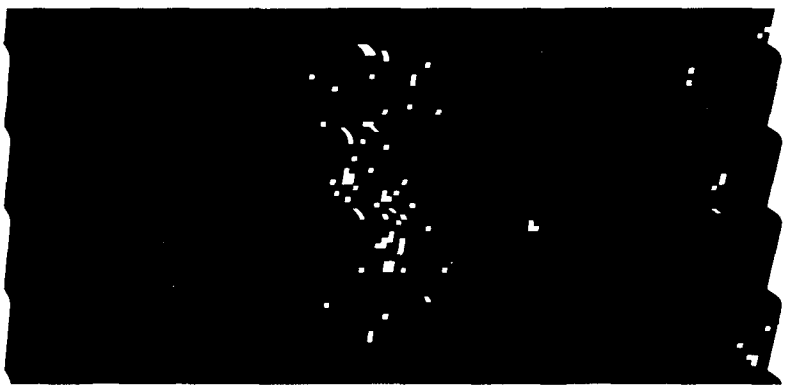

Figure 66. *Segmented M98F09 Culture All Polarizations WS 8 × 8*

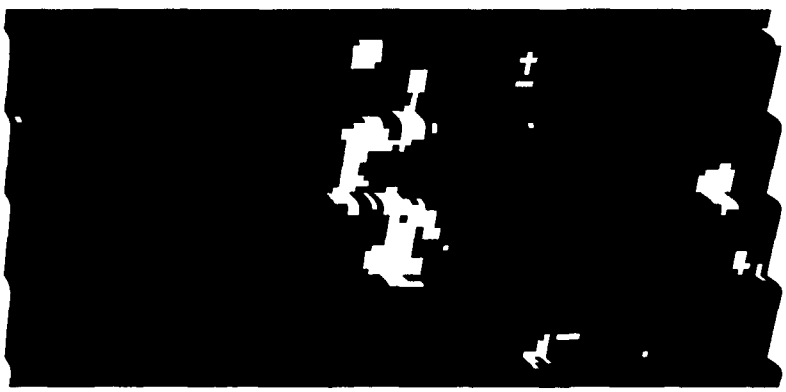

Figure 67. Segmented M98F09 Culture Median Filtered HH Polarization WS 8 × 8

4.9.3 **M98F10 Subjective Evaluation** The final frame that was subjectively evaluated was M98F10. Figure 68 is the HH polarization image of this frame. This image contains a corner reflector calibration site along with various other camouflage experiments. The exact locations of these experiments were unknown. Ground truth photographs indicated the presence of camouflage nets both tented and lying on the ground. Portions of the field where the calibration array was place had been mowed. Figure 69 is the correlation dimension image of this frame calculated using all polarizations and a window size of 16×16. The lower correlation dimension values correspond to the location of cultural objects within the frame. Figure 70 is a 1024×512 corner reflector template for this frame. Shown in Figure 71 is the 64×32 corner reflector template. The image shown in Figure 72 is a result of thresholding the correlation dimension image to separate the cultural objects. The location of the cultural objects indicated in Figure 72 correspond closely to the corner reflector template. Three additional regions were also identified as culture. From the photographs of the site there is a strong possibility that these regions correspond to the camouflage experiments. Shown in Figure 73 is the result of setting the threshold at the tree–field threshold value and then performing a median filter operation. An interesting result is observed. While the tall grass and the short grass possess the same values of correlation dimension the boundary between the tall grass and the short grass exhibit lower correlation dimension values. Also the areas surrounding the corner reflector locations and possibly the other experiments possess lower correlation dimension values. Without detailed ground truth of a large quantity of data the conclusion that areas trampled down by the presence of man possess a lower correlation dimension would be impossible to verify.

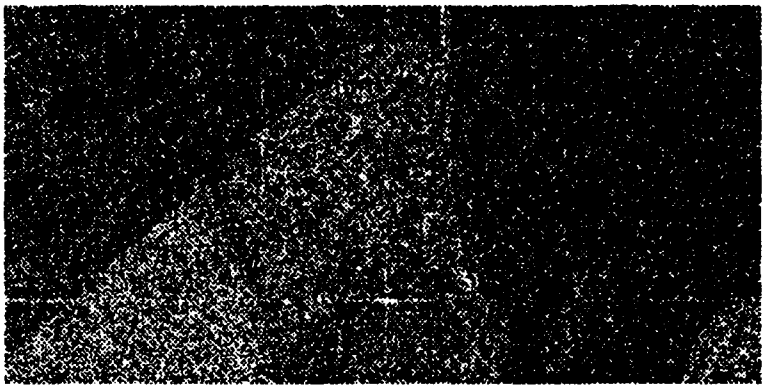

Figure 68. M98F10 HH Polarization 1024 × 512

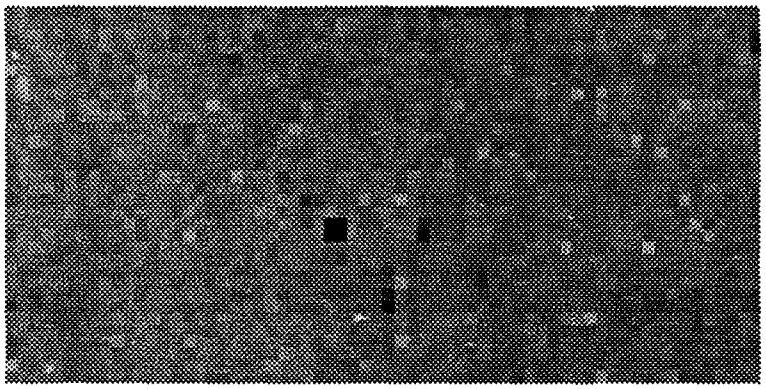

Figure 69. M98F10 Correlation Dimension Values ×96 All Polarizations WS 16×16

Figure 70. M98F10 Corner Reflector Template 1024 × 512

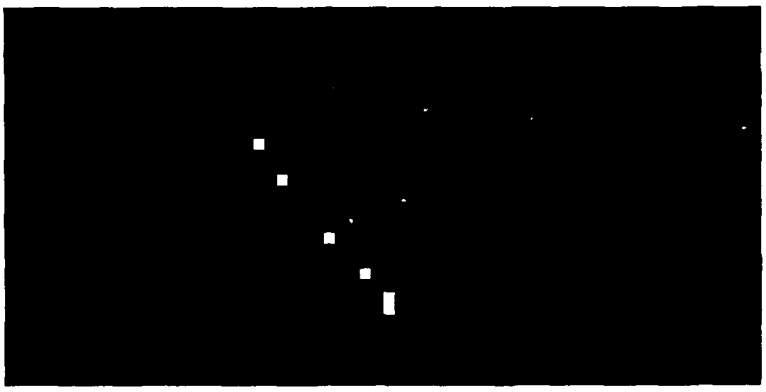

Figure 71. M98F10 Corner Reflector Template 64 × 32

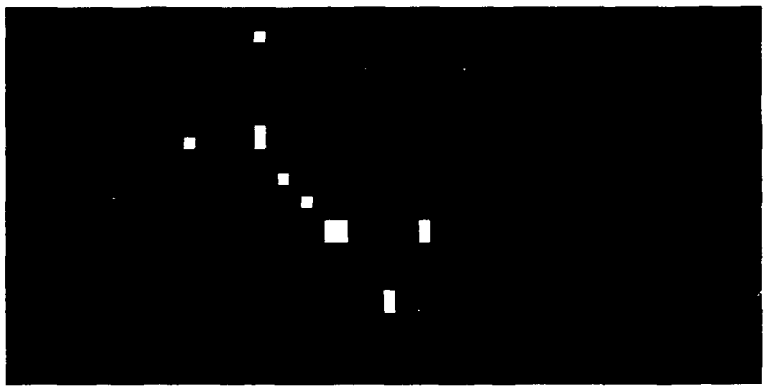

Figure 72. Segmented M98F10 Corner Reflectors All Polarizations WS 16 × 16

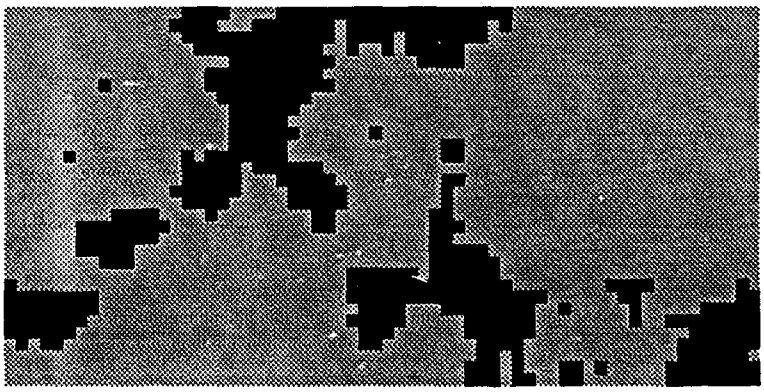

Figure 73. Segmented M98F10 Corner Reflectors/Tall-Short Grass Boundary All Polarizations WS 16 × 16

4.10 Neural Network Results

In this section the results of using correlation dimension estimates calculated using different combinations of polarizations as features to train an ANN will be discussed.

> There is nothing mysterious or magic about neural networks, nothing up the sleeve, there are sets of equations that describe what the artificial neural networks are going to do (22).

The above statement is one made often by Dr Steve Rogers when discussing artificial neural networks. However, this researcher has come to the conclusion that implementing a neural network is an art and not a science. Individuals that use and teach neural networks on a daily basis each have their own preference on the kind of neural network to implement for a given data set. The choice of which neural network to implement is more a religious choice than a scientific one. The correlation dimension values generated during this thesis were applied to two different types of ANN the Kohonen and the radial basis function.

4.10.1 Kohonen Neural Network A Kohonen neural network was chosen to incorporate the correlation dimension estimates from all combinations of polarizations into one segmented image. The basis for this choice was the recommendation of several individuals knowledgeable on Kohonen networks, the need to cluster data in an unsupervised manner and the availability of proven code. The program written by Recla and Barmore was converted from VMS to UNIX and DOS, then the program was validated on sample data to ensure accurate results. Several additional programs were written to develop a system capable of end–to–end training, calibrating, and testing of the Kohonen neural network. After the system was developed the task of finding the right combination of Kohonen parameters to use to produce an acceptable segmented image was undertaken. The goal was to train a neural network to recognize vectors whose elements were made up of correlation dimension

estimates from the various combination of polarizations and then have that network produce results that were more accurate than one correlation dimension alone. The following parameters were variables that could be changed:

- number/combination of input features
- size of output Kohonen layer
- gain reduction method
- conscience value (if used)
- number of iterations

A problem arose when trying to calibrate the trained Kohonen layer to determine which node on the output Kohonen layer was assigned to particular class of data. In all the Kohonen networks that were trained there were several ambiguous nodes. Ambiguous nodes are nodes that win for more than one class of input data. Ambiguous nodes would win whether tree or field vectors were applied to the input. Several months of research effort was expended in an effort to find the proper combination of Kohonen parameters required to accomplish the goal. All images created using this method demonstrated poor segmentation. This researcher's inability to train a Kohonen neural network using correlation dimension estimates as features does not prove that a Kohonen neural network is not capable of segmenting this data. However, it does indicate that training a Kohonen neural network is not a trivial exercise.

4.10.2 **Radial Basis Function** Three hundred vectors created using correlation dimension estimates from two different combinations of the fifteen possible combinations of polarizations were used to train RBF neural networks developed by Dan Zihirniak (31). These training vectors consisted of 100 vectors each of tree, field and shadow regions. The first polarization combination was correlation dimension

Table 10. Radial Basis Function Output Evaluation

Percentage Matching Image Truth Template		
Image Evaluated	Using 4 Correlation Dimension Features	Using 15 Correlation Dimension Features
Msn 85 F27	78.3	79.6
Msn 85 F28	93.0	92.5
Msn 98 F07	99.6	98.8
Msn 98 F08	85.6	88.0
Msn 98 F11	93.3	91.7
Msn 98 F12	95.6	94.9
Mean	90.9	90.9

estimates from all fifteen different combinations of polarizations. The second combination was a subset of the first. Instead of using all fifteen combinations, only four correlation dimension features representative of the entire set were used. The four combinations in the second set were HH, HH & HV, HH & VH & VV, and HH & HV & VH & VV.

Shown in Figure 74 are the three regions where the 100 training vectors from the two polarization combinations were obtained. The RBF networks were trained with the RBF centers chosen via the center class average method. After training the RBF networks with vectors from the three regions indicated in Figure 74 vectors from all six images containing only naturally occurring regions (tree, field, shadow) were processed with the trained networks. Shown in Table 4.10.2 are the results of performing a pixel by pixel comparison between the resulting RBF output and the image truth templates for each frame. Results using four correlation dimension features and fifteen correlation dimension features are provided.

The mean for all images using both four correlation features and fifteen correlation features was 90.9%. Again, Mission 85 Frame 27 contained the lowest percentage correct. As discussed earlier, the image truth templates were not 100% accurate. Using both four correlation features and fifteen correlation features produced very

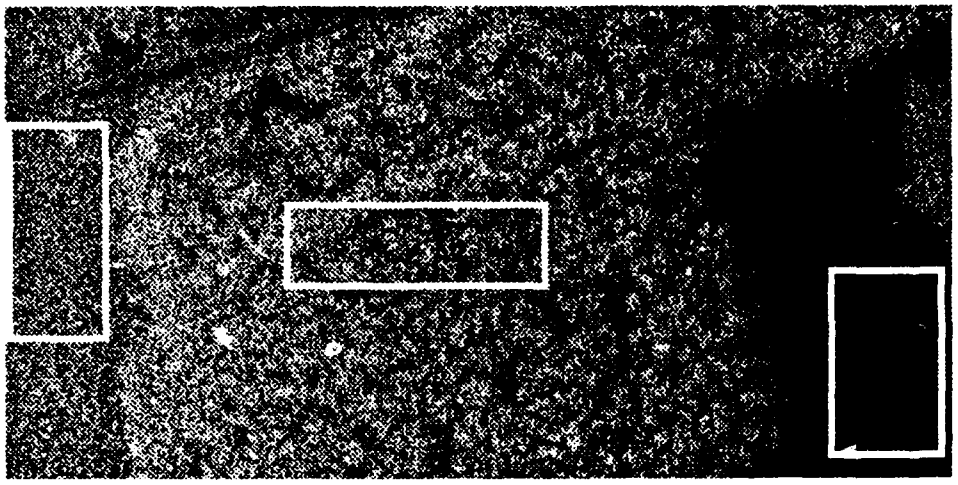

Figure 74. M85F28 RBF Training Regions

accurate results. These results were obtained by training on vectors from Mission 85 Frame 28 and then testing on frames from both Mission 85 (New York collection) and Mission 98 (Maine collection). The RBF was able to generalize and identify the regions across all images.

The RBF networks used had many different parameters that could have been varied to improve performance. The RBF function was not optimized. Trying to optimize the RBF network without exact image truth templates was considered pointless. Also, if the objective was to train an RBF to get the maximum percentage possible correct the method used here to chose the training vectors would not have been used. Rather than using a block of contiguous vectors as training vectors, a judicious selection process would have been implemented to choose 100 training vectors from each class that best represented the image data. For instance, more training vectors would have been chosen around the boundaries between regions since this was the area most often misclassified.

Shown in Figure 75 - 92 are the resulting segmented images produced by the RBF networks. The use of RBF networks has demonstrated that correlation dimension estimates are robust features to use for SAR image segmentation.

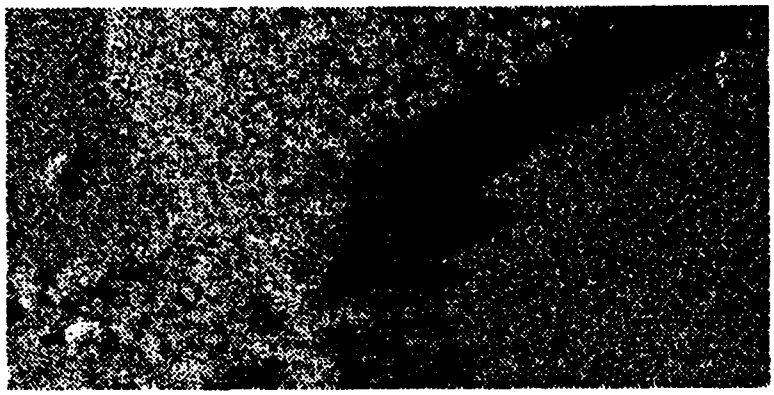

Figure 75. M85F27 HH Polarization 1024 × 512

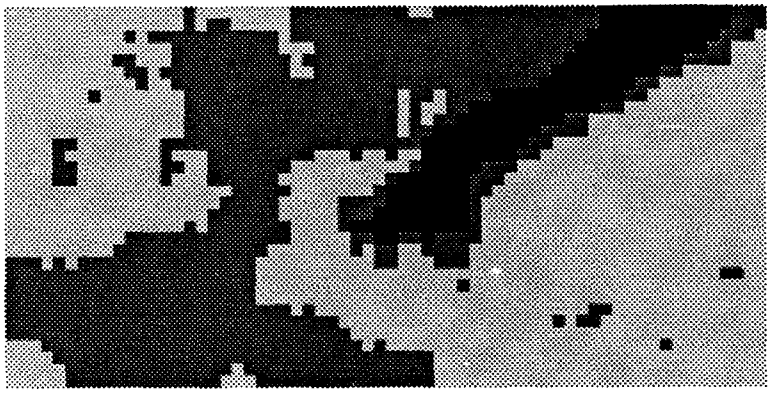

Figure 76. M85F27 RBF Output (15 Features) WS 16 × 16

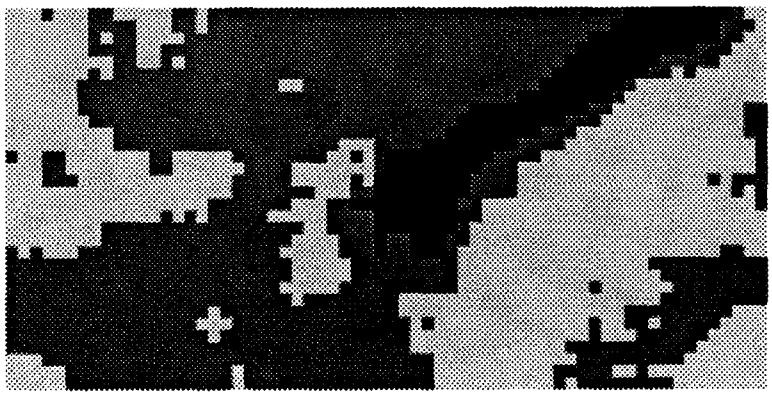

Figure 77. M85F27 RBF Output (4 Features) WS 16 × 16

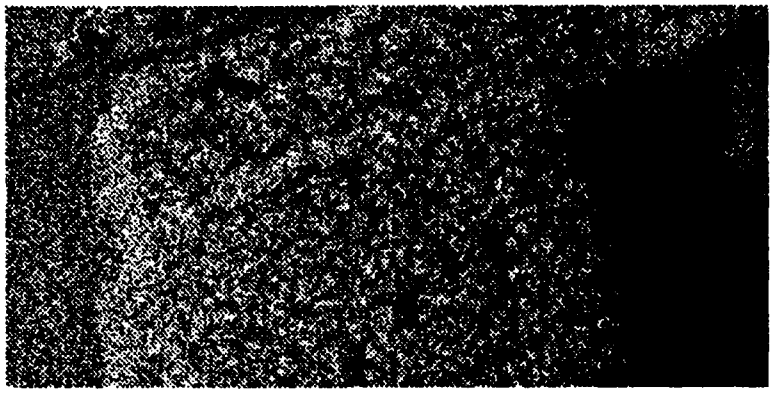

Figure 78. M85F28 HH Polarization 1024 × 512

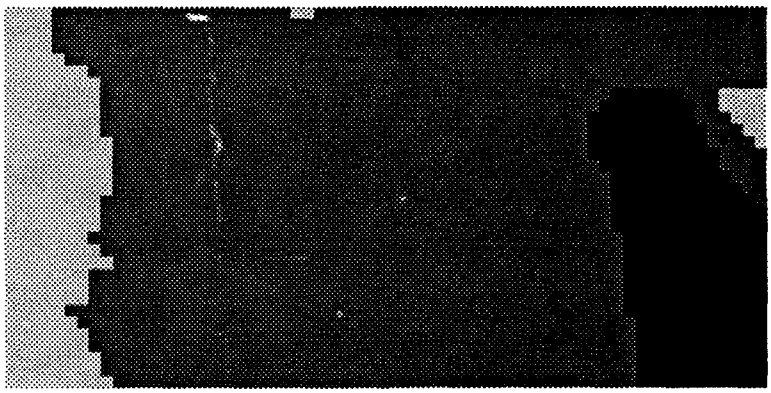

Figure 79. M85F28 RBF Output (15 Features) WS 16 × 16

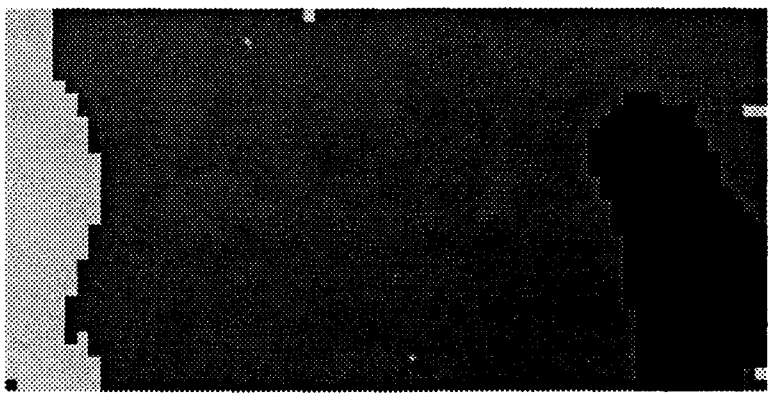

Figure 80. M85F28 RBF Output (4 Features) WS 16 × 16

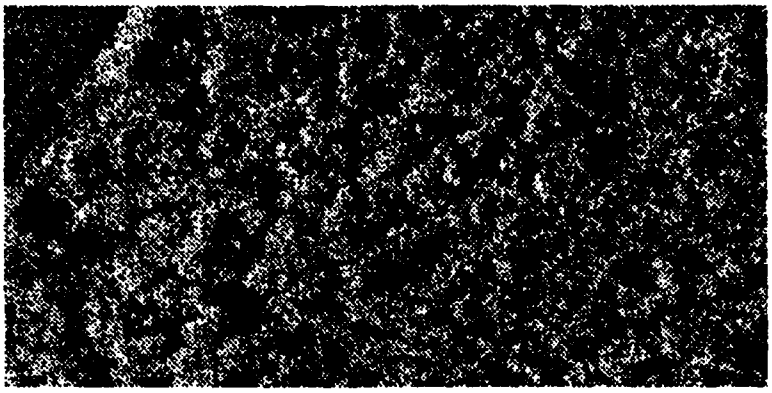

Figure 81. M98F07 HH Polarization 1024 × 512

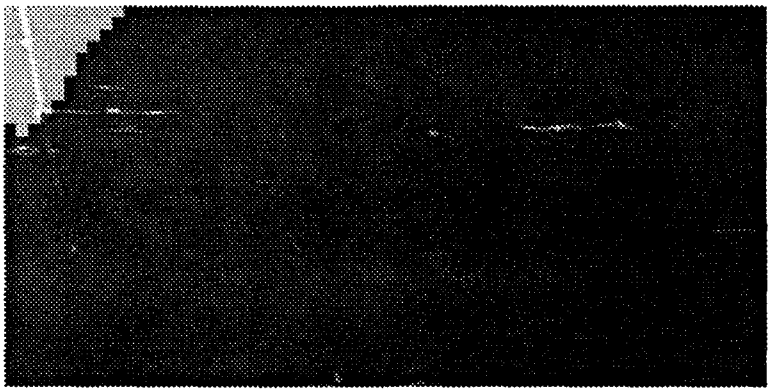

Figure 82. M98F07 RBF Output (15 Features) WS 16 × 16

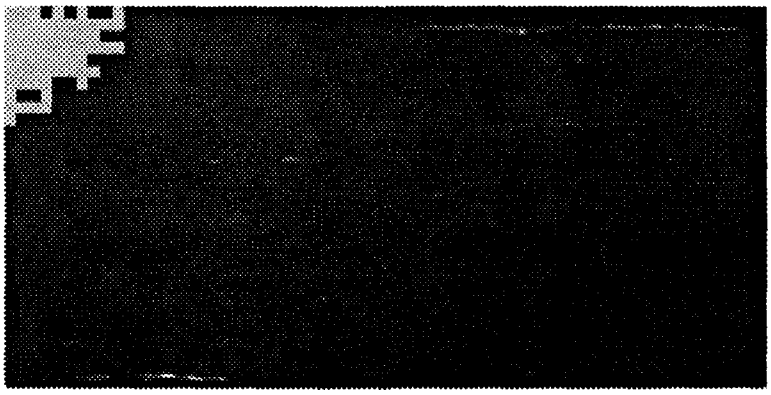

Figure 83. M98F07 RBF Output (4 Features) WS 16 × 16

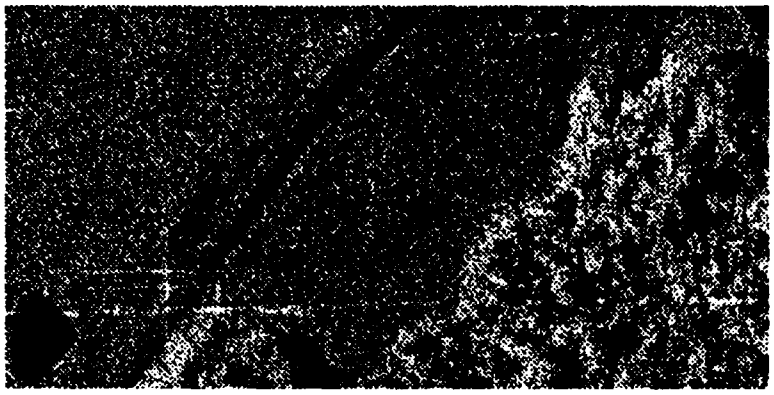

Figure 84. M98F08 HH Polarization 1024 × 512

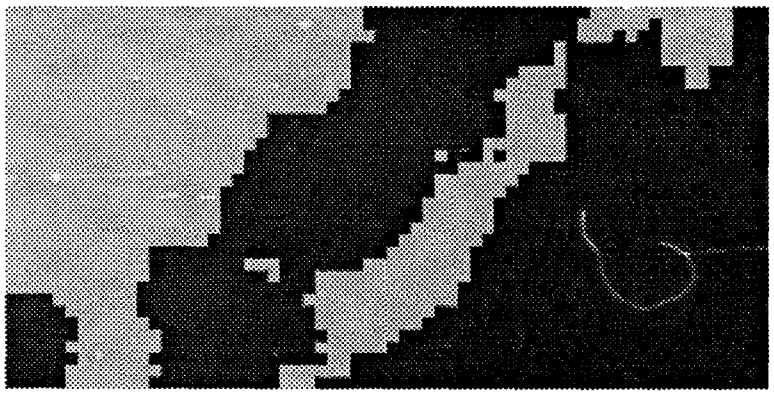

Figure 85. M98F08 RBF Output (15 Features) WS 16 × 16

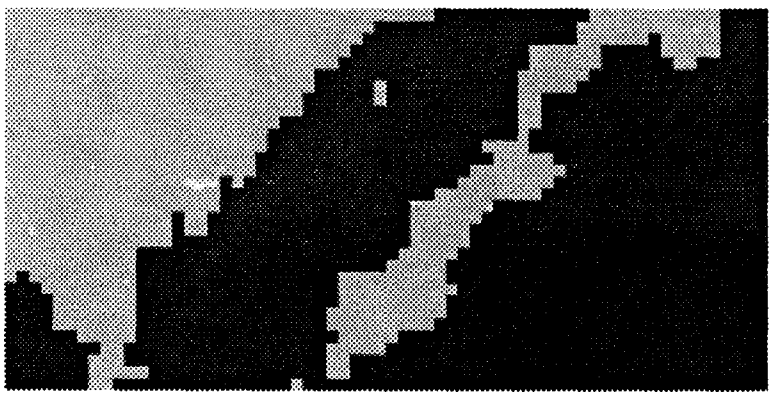

Figure 86. M98F08 RBF Output (4 Features) WS 16 × 16

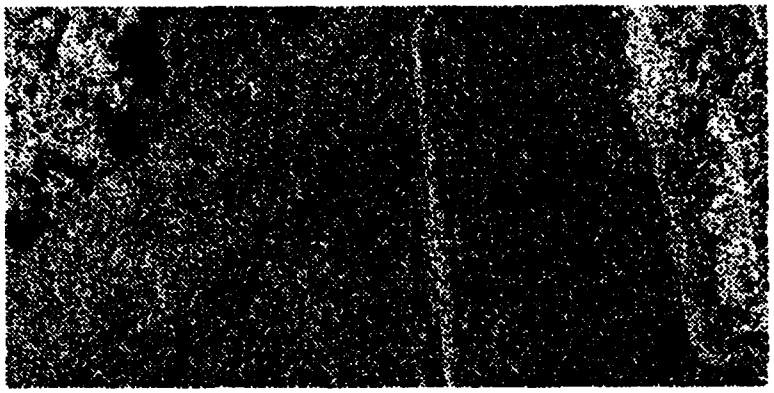

Figure 87. M98F11 HH Polarization 1024 × 512

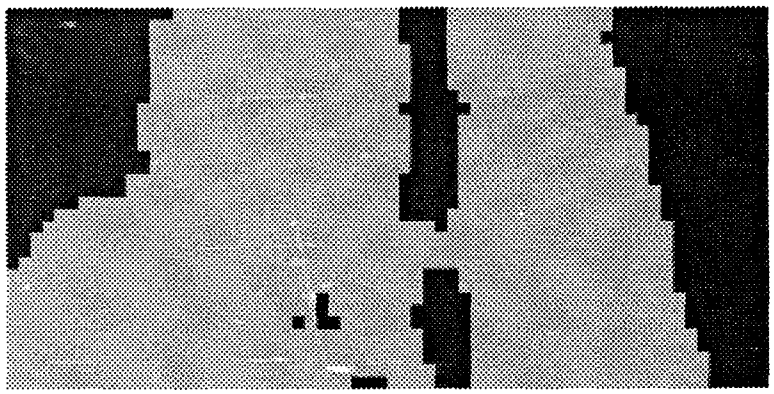

Figure 88. M98F11 RBF Output (15 Features) WS 16 × 16

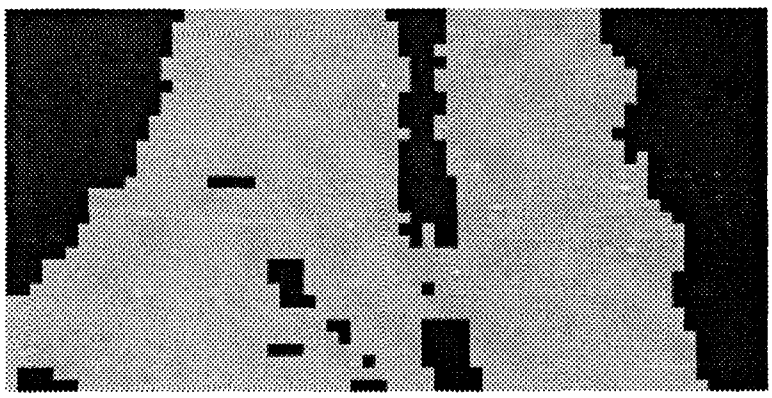

Figure 89. M98F11 RBF Output (4 Features) WS 16 × 16

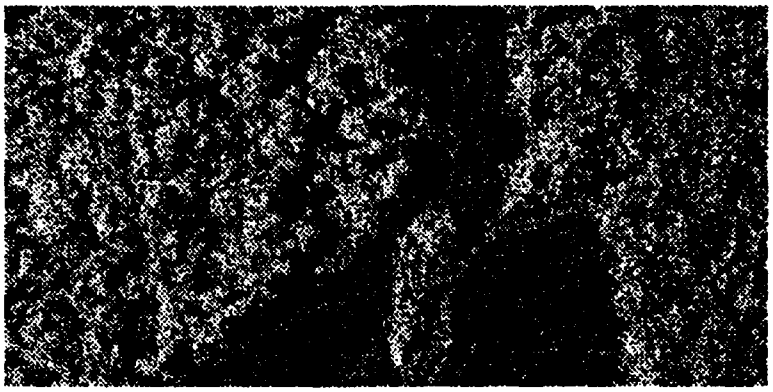

Figure 90. M98F12 HH Polarization 1024 × 512

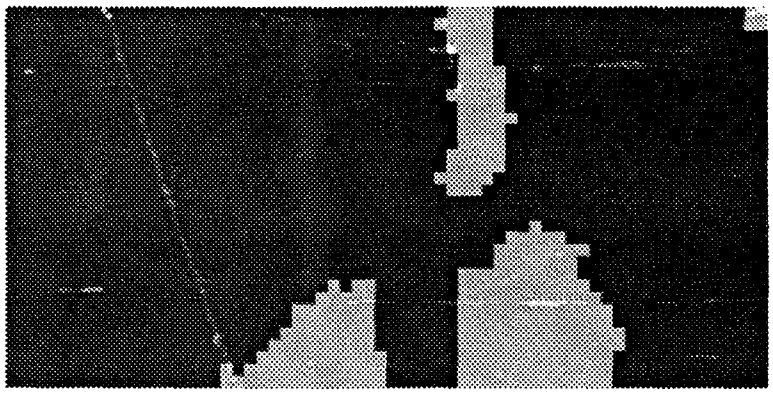

Figure 91. M98F12 RBF Output (15 Features) WS 16 × 16

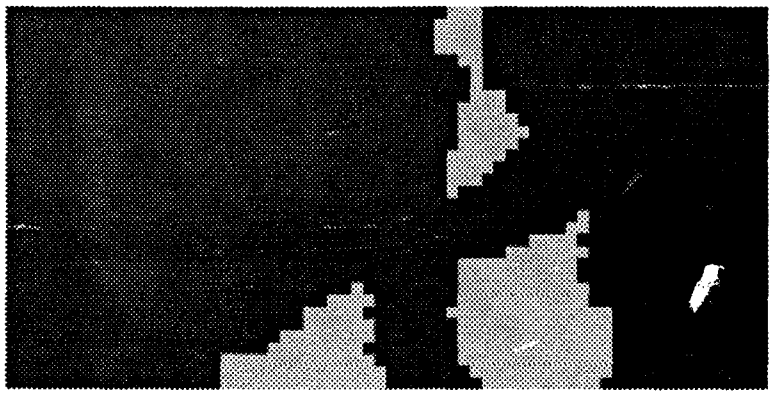

Figure 92. M98F12 RBF Output (4 Features) WS 16 × 16

4.11 Summary

In this chapter the results of estimating the correlation dimension of polarimetric SAR imagery has been presented. From the limited amount of data processed the following conclusions appear to hold:

- Correlation dimension values alone appear adequate to segment between tree, field, shadow, and cultural regions contained in polarimetric SAR imagery.
- Correlation dimensions calculated using a window size of 16×16 provide higher percentages correct than when a window size of 8×8 was used.
- Thresholds used to separate between two regions of a correlation dimension image generated using a particular combination of polarizations and a particular window size hold across images, missions, and parts of the country for all correlation dimension images calculated using the same polarizations and window size.
- The use of polarimetric data increases the accuracy of correlation dimension segmentation.
- Correlation dimension estimates were used successfully as features to train radial basis function neural networks to distinguish automatically between between different naturally occurring regions within a SAR image.

Based on the above conclusions correlation dimension estimates appear to be a valid feature to incorporate into a polarimetric SAR segmentation scheme.

V. Conclusion and Recommendations

5.1 Introduction

This thesis effort was aimed at investigating the potential of correlation dimension estimation to segment polarimetric SAR imagery. This chapter provides a general overview to the results achieved during this research effort. Also provided are recommendations regarding areas of investigation for future researchers.

5.2 Overall Results

The objective of this thesis was to answer the following questions:

- Can fractal geometry be used to effectively segment high resolution polarimetric SAR imagery into natural and cultural regions?
- Do naturally occurring regions within a SAR image exhibit values of correlation dimension estimates that can be used to separate between the regions?
- Does the use of polarimetric SAR data instead of non–polarimetric data improve the ability to segment images using correlation dimension estimation?
- Can an artificial neural network be trained to segment SAR imagery automatically using correlation dimension estimates as features?

Based on the results obtained during this research endeavor the following answers are provided to the above questions:

- Cultural objects appear to possess lower correlation dimension estimates than naturally occurring regions. Using correlation dimension estimates alone provides the ability to detect where man–made objects are located in a SAR scene.
- Using simple thresholding and median filtering of correlation dimension values calculated from SAR imagery produced segmented images that were consistently 90% accurate when using all four polarizations.

- The use of multiple combinations of polarizations from a particular frame increased the probability of segmenting the SAR imagery.
- Radial basis function neural networks provided a method to quickly and accurately segment SAR imagery into different naturally occurring regions using correlation dimension estimates as features. These trained networks were capable of generalizing over SAR imagery collected on different missions and different regions of the country.

The purpose of this research was to investigate the potential of using fractal geometry, particularly correlation dimension estimation, to segment SAR imagery. The goal was not to design a complex SAR segmenter. The approach used to evaluate the potential of using correlation dimension estimates to segment high resolution polarimetric SAR data was unsophisticated. However, even with this simple approach remarkably accurate segmented images were produced. The results presented in this thesis demonstrate that correlation dimension estimation is a valid method to use for SAR image segmentation.

5.3 Recommendations for Future Research

The following suggestions are provided to anyone interested in furthering this investigation into the application of correlation dimension estimation to pattern recognition research involving SAR imagery.

- The conclusions reached during this thesis effort were limited to the accuracy of the ground truth data available. Accurate ground truth documentation of the sites imaged by the SAR radar is necessary to evaluate precisely the results obtained using correlation dimension estimation. Obtain detailed documentation of the sites prior to image selection.
- The window sizes used to calculate the correlation dimension estimates were non–overlapping. Using non–overlapping windows resulted in reduced resolu-

tion for the resulting segmented image. The use of overlapping windows can be used to increase the apparent resolution obtained during this procedure. Probably the best results could be obtained using a sliding window that moved one pixel at a time. However, the price paid for the increased resolution is longer computation time.

- This research focused on using primarily the I and Q representation of SAR imagery. A detailed investigation using the magnitude/phase representation of SAR imagery is required before concluding that the I and Q representation provides more accurate results. The code written for this thesis, (FRACTAL.c), has the ability to calculate correlation dimension based on either representation of the SAR data.
- Design a sophisticated SAR image segmentation system incorporating correlation dimension estimates as a feature. A tremendous amount of research has been conducted regarding the development of image segmenters. By merging the results obtained from this thesis effort with pattern recognition research a system capable of providing extremely accurate segmentation could result.
- Radial Basis Function neural networks demonstrated great potential as a method for automatically identifying regions using correlation dimension estimates as inputs. Additional research is required to specify the optimum parameters and input features required for a radial basis function.

5.4 Summary

The goals of this thesis were met. Correlation dimension estimates are valid features for segmenting high resolution polarimetric SAR data. Multiple areas requiring additional research have been identified. Investigation of fractal geometry applications holds great promise for solving many of the unsolved pattern recognition problems that exist today.

Appendix A. **Conversion To SUN Format**

The data used during this research consisted of the I and Q components of each polarization that had been converted to 8-8-4 compressed format and stored on 2.3 Gigabyte 8 mm Exabyte Tape using the VMS operating system. Several steps were required in order to decompress the imagery and convert it to a format useable on UNIX and DOS operating systems. Table 11 shows the steps necessary to convert the 8-8-4 format data into float values useable on UNIX systems. Several of these steps would have been unnecessary if the available VMS system had had a 2.3 Gigabyte 8 mm Exabyte tape system installed or if a method to convert the VAX compressed 8-8-4 format to SUN float values had existed.

Table 11. Conversion From VMS 8-8-4 Format to UNIX Format

Step 1	Read Exabyte tape using UNIX system
Step 2	Transfer files to VMS system via 9 track tape
Step 3	Uncompress on VMS system using programs provided by MITLL into VMS complex-8 format
Step 4	Transfer to UNIX via 9 Track Tape
Step 5	Convert VMS complex-8 format into UNIX float format

Appendix B. **Fractal.C**

```
/*********************************************************************
  DATE: 15 July 1990
  VERSION: 15.5
  NAME: Fractal.C
  DESCRIPTION: This program calculates the correlation dimension estimate
               of individual non-overlapping windows of a SAR image based
               on Euclidean distances between magnitudes, phases, or both
               magnitudes or phases representing a pixel.  The input files
               contain I and Q components of an image in float values.
  FILES READ: FxxHH.sun   These files contain the I and Q components of
              FxxHV.sun   polarimetric SAR imagery.  Program is capable
              FxxVH.sun   of handling any combination of these
              FxxVV.sun   polarizations.

  FILES WRITTEN:  Fxx(polarizations).flt  This file contains the correlation
                                          dimension estimates of the SAR image
                                          based on window size and polarizations
                                          chosen.  (float format)
  AUTHORS: Algorithm written by Joseph Brickey, Extensive programming
           modifications by Michael Bryant and Kevin Wiley
*********************************************************************/
#include <stdio.h>
/*#include <sys/stat.h>*/ /* for DOS use only */
#include <math.h>
#include <fcntl.h>
/*#include <unistd.h>*/   /* for DOS use only */

/* Global Definitions */
#define IMAGE_WIDTH 1024 /* full image size */
#define IMAGE_HEIGHT 512
#define WINDOW_SIZE 16 /* window is square */
#define NDATA 25
#define PI 3.14159265
#define SEEK_CUR 1
#define SEEK_SET 0
#define CELL_OFFSET (IMAGE_WIDTH - WINDOW_SIZE)
#define window_high_image_width WINDOW_SIZE * IMAGE_WIDTH
#define dist_dim  (WINDOW_SIZE*WINDOW_SIZE*WINDOW_SIZE*WINDOW_SIZE -
                   WINDOW_SIZE*WINDOW_SIZE)/2

struct cmplx
{
float real, imag;
};

struct phasor
{
float mag, phase;
};

int ndatat;
float aa, abdevt, *xt, *yt;


/*********************************************************************
FUNCTIONS
*********************************************************************/
```

```
int compare_floats (elem1, elem2)
float *elem1, *elem2;
{
if (*elem1 < *elem2) return(-1);
if (*elem1 > *elem2) return(1);
return(0);
}

/*************************************************************************/
/* Sub-routine to read I and Q components of individual window          */
void Read_block(sar_file, seek_cell, block)
int sar_file;
long seek_cell;
struct cmplx *block;
{
int row, row_bytes = WINDOW_SIZE * sizeof(struct cmplx);
unsigned next_row_offset = CELL_OFFSET * sizeof(struct cmplx);
        long bytes_read;

if (lseek(sar_file, seek_cell, SEEK_SET) == -1L)
{
fprintf(stderr, "Seek error in Read_block\n");
exit(1);
}

for (row = 0; row < WINDOW_SIZE; ++row)
{
         bytes_read = read(sar_file, block, row_bytes);
if ( bytes_read != row_bytes)
{
fprintf(stderr, "Read error in Read_block\n");
printf("seek_cell = %ld, bytes_read = %ld\n",
seek_cell, bytes_read);
exit(1);
}
                block += WINDOW_SIZE;
                if(lseek(sar_file, next_row_offset, SEEK_CUR) == -1L)
{
fprintf(stderr, "Seek error in Read_block\n");
exit(1);
}
}
}

/*************************************************************************/
/* Sub-routine to write correlation dimension value (slope) to a file    */
void Write_results(result_file, slope)
int result_file;
float slope;
{
write(result_file, &slope, sizeof(float));
}

/*************************************************************************/
/* Sub-routine to calculate magnitude and phase from I and Q components  */
float Cmplx_to_Phasor(c_block, p_block)
struct cmplx *c_block;
struct phasor *p_block;
{
float max_mag = 0.0;
int i, i_max = WINDOW_SIZE*WINDOW_SIZE;

for (i = 0; i < i_max; ++i)
{
p_block->mag = sqrt((c_block->real * c_block->real) +
```

```
    (c_block->imag * c_block->imag));

if (p_block->mag > max_mag) max_mag = p_block->mag;

                if(p_block->mag > 0.0)
p_block->phase = atan2(c_block->imag, c_block->real);
else
p_block->phase = 0.0;

++c_block;
                ++p_block;
}
        return (max_mag);
}

/*************************************************************************/
/* Sub-routine to scale magnitudes and phases to fill window            */
void Scale(p_block, max_mag, vector)
struct phasor *p_block;
float max_mag;
struct phasor *vector;
{
int i, i_max = WINDOW_SIZE*WINDOW_SIZE;
float mag_scale = WINDOW_SIZE/max_mag;
  float phase_scale = WINDOW_SIZE/(2 * PI);

for (i = 0; i < i_max; ++i)
{
    vector->mag = c_block->mag * mag_scale;
    vector->phase = c_block->phase * phase_scale;
++c_block;
++vector;
}
}

/*************************************************************************/
/* Sub-routine to calculate Euclidean distance between magnitudes,      */
/* phases, or both magnitudes and phases based on polarizations used.   */

float Calc_dist(vector, dist_vector, m_or_p, num_files)
struct phasor **vector;
float dist_vector[];
int *m_or_p;
{
unsigned first, second;
unsigned i = 0, j;
unsigned max_count = WINDOW_SIZE * WINDOW_SIZE;
float max_distance = 0.0;
for (first = 0; first < max_count; ++first)
        {
for (second = first + 1; second < max_count; ++second)
{
dist_vector[i] = 0.0;
for(j=0; j<num_files; ++j)
{
switch(m_or_p[j])
{
case 'b' :
{
dist_vector[i] +=
(vector[j][first].mag -
vector[j][second].mag) *
(vector[j][first].mag -
vector[j][second].mag);
                                        }
```

```
case 'p' :
{
dist_vector[i] +=
(vector[j][first].phase -
vector[j][second].phase) *
(vector[j][first].phase -
vector[j][second].phase);
break;
                                        }
case 'm' :
{
dist_vector[i] +=
(vector[j][first].mag -
vector[j][second].mag) *
(vector[j][first].mag -
vector[j][second].mag);
                                        }
                                    }
}
dist_vector[i] = sqrt(dist_vector[i]);
if(dist_vector[i]>max_distance)
max_distance = dist_vector[i];
i++;
                }
        }
        return(max_distance);
}

/*********************************************************************/
/* Sub-routine to calculate log(r) and log(c) to be used to find slope   */
int Calc(dist_vector, logr, logc, max_dist)
float dist_vector[], logr[], logc[], max_dist;
{
int last = NDATA - 1;
int i, j;
float r[NDATA], c[NDATA], factor = NDATA / max_dist - 0.000001;
float interval = max_dist/NDATA;
int zeroes = 0;

for(i=0; i<=last; i++)
{
r[i] = (i+1)*(interval);
c[i] = 0;
        }

for(j=0; j<dist_dim; j++)
{
i = (int)(dist_vector[j] * factor);
++(c[i]);
}

        c[0] *= 2;
for(j=1; j<NDATA; j++)
c[j] = c[j-1] + c[j] * 2;
        c[24] -= 2;
for(i=0; i<NDATA; i++)
        {
if(c[i]>0)
{
zeroes = i;
break;
}
        }
for(i=0; i<NDATA-zeroes; i++)
{
```

```
logr[i] = log(r[i+zeroes]);
logc[i] = log(c[i+zeroes]);
}
return(zeroes);
}

/*************************************************************************/
/* The following two sub-routines rofunc and medfit are used to          */
/* calculate the slope of the line of c vs r by weighted least squares   */
float rofunc(b)
float b;

{
int j,n1,nmh,nml;
float arr[NDATA],d,sum=0.0;

n1=ndatat+1;
nml=n1/2;
nmh=n1-nml;
for (j=0;j<ndatat;j++)
arr[j]=yt[j]-b*xt[j];
qsort(arr, ndatat, sizeof(float), compare_floats);
aa=0.5*(arr[nml-1]+arr[nmh-1]);
abdevt=0.0;
for (j=0;j<ndatat;j++)
{
d=yt[j]-(b*xt[j]+aa);
abdevt += fabs(d);
sum += d > 0.0 ? xt[j] : -xt[j];
}
return sum;
}


float medfit(x,y,ndata)
float x[], y[];
int ndata;
{
int j;
float bb=0.0,b1=0.0,b2=0.0,del=0.0,f=0.0,f1=0.0,f2=0.0,sigb=0.0,temp=0.0;
float sx=0.0,sy=0.0,sxy=0.0,sxx=0.0,chisq=0.0;

ndatat=ndata;
xt=x;
yt=y;
for (j=0;j<ndata;j++) {
sx += x[j];
sy += y[j];
sxy += x[j]*y[j];
sxx += x[j]*x[j];
}
del=ndata*sxx-sx*sx;
aa=(sxx*sy-sx*sxy)/del;
bb=(ndata*sxy-sx*sy)/del;
for (j=1;j<=ndata;j++)
chisq += (temp=y[j]-(aa+bb*x[j]),temp*temp);
sigb=sqrt(chisq/del);
b1=bb;
f1=rofunc(b1);
b2=bb+((f1 > 0.0) ? fabs(3.0*sigb) : -fabs(3.0*sigb));
f2=rofunc(b2);
while (f1*f2 > 0.0) {
bb=2.0*b2-b1;
b1=b2;
f1=f2;
```

```
b2=bb;
f2=rofunc(b2);
}
sigb=0.01*sigb;
while (fabs(b2-b1) > sigb) {
bb=0.5*(b1+b2);
if (bb == b1 || bb == b2) break;
f=rofunc(bb);
if (f*f1 >= 0.0) {
f1=f:
b1=bb;
} else {
f2=f;
b2=bb;
}
}
return(bb);
}

/*************************************************************************/
void main(argc, argv)
int argc;
char *argv[];
{
char in_fname[4][40], out_fname[40];
int in_file[4], out_file;
        long block_pointer;
unsigned block_row, block_col, block_row_max, block_col_max;
struct cmplx RI_block[WINDOW_SIZE][WINDOW_SIZE];
struct phasor MP_block[WINDOW_SIZE][WINDOW_SIZE];
struct phasor **vector;
        struct phasor *vec_rows[4];
struct phasor vec_elems[4][WINDOW_SIZE * WINDOW_SIZE];
float dist_vector[(WINDOW_SIZE*WINDOW_SIZE*WINDOW_SIZE*WINDOW_SIZE
   - WINDOW_SIZE*WINDOW_SIZE)/2];
float max_mag, max_dist, zeroes;
float r[NDATA], c[NDATA], logr[NDATA], logc[NDATA];
float slope;
int temp, num_files, m_or_p[4], i;
        FILE *log_data;

for(i=0; i<4; ++i) vec_rows[i] = &vec_elems[i][0];
vector = &vec_rows[0];

num_files = argc / 2 - 1;
for(i=0; i<num_files; ++i)
{
switch(argv[i*2+1][0])
{
case 'm' :
{
m_or_p[i] = 'm';
break;
}
case 'p' :
{
m_or_p[i] = 'p';
break;
}
case 'b' :
{
m_or_p[i] = 'b';
break;
}
default :
```

```
{
printf("Usage : frac (m|p|b in_file)... out_file\n");
exit(1);
}
                }
strcpy(in_fname[i],argv[i*2+2]);
}

strcpy(out_fname,argv[argc-1]);

for(i=0; i<num_files; ++i)
if((in_file[i] = open(in_fname[i], O_RDONLY ))== -1)
{
printf("Error opening input file %d \n", i);
exit(1);
}
  if ((out_file = open(out_fname, O_CREAT | O_WRONLY , 0444)) == -1)
{
printf("Error opening output file \n");
exit(1);
        }

/*if ((log_data = fopen("LOG.PRN", "wt")) == NULL)
{
   fprintf(stderr,"Cannot open output file.\n");
   exit(1);
}*/

block_row_max = IMAGE_HEIGHT / WINDOW_SIZE;
block_col_max = IMAGE_WIDTH / WINDOW_SIZE;

for(block_row=0; block_row < block_row_max; block_row++)
{
             /*   printf("block_row = %d\n", block_row);*/
for(block_col=0; block_col < block_col_max; block_col++)
{
block_pointer = (long)(block_col * WINDOW_SIZE +
 block_row * window_high_image_width)
           * sizeof(struct cmplx);
for(i=0; i<num_files; ++i)
                        {
Read_block(in_file[i], block_pointer, &RI_block[0][0]);
max_mag = Cmplx_to_Phasor(&RI_block[0][0],
  &MP_block[0][0]);
       Scale(&MP_block[0][0], max_mag, &vec_elems[i][0]);
                        }
max_dist = Calc_dist(vector, dist_vector, m_or_p, num_files);
zeroes = Calc(dist_vector, logr, logc, max_dist);
temp = NDATA-zeroes;
/^for(i=0; i<NDATA; ++i)
{
fprintf(log_data,"%f,%f\n", logr[i], logc[i]);
}*/
slope = medfit(logr, logc, temp);
/*printf("slope = %f \n", slope);*/
Write_results(out_file, slope);
}
}
fclose(log_data);
}
```

Bibliography

1. Barmore, Gary D. *Speech Recognition Using Neural Nets and Dynamic Time Warping*. MS thesis, School of Engineering, Air Force Institute of Technology (AU), Wright Patterson AFB, OH, December 1988.
2. Barnsley, Michael F. *Fractals Everywhere*. San Diego: Academic Press, Inc, 1988.
3. Bingham, Stuart C. and Mark Kot. *Multidimensional Trees, Range Searching, and a Correlation Dimension Algorithm of Reduced Complexity*. Technical Report, University of Tennessee, April 1989.
4. Bohr, Niels Henrik. *Atomic Theory and the Description of Nature*. London: Cambridge University Press, 1934.
5. Farmer, J. D. and others. "The Dimension of Chaotic Attractors," *Physica*, *7D*:153–180 (1983).
6. Gleick, James. *Chaos: Making a New Science*. Harrisburg, VA: R.R. Donnelley and Sons Company, 1987.
7. Gonzalez, Rafael C. and Paul Wintz. *Digital Image Processing* (second Edition). Reading, Massachusetts: Addison-Wesley Publishing Company, Inc., 1987.
8. Grassberger, P. and I. Procaccia. "Dimensions and Entropies Of Strange Attractors From A Fluctuating Dynamics Approach," *Physica*, *13D*:34–54 (May 1984).
9. Grassberger, Peter and Itmar Procaccia. "Measuring The Strangeness of Strange Attractors," *Physica*, *9D*:189–208 (May 1983).
10. Hentschel, H.G.E. and Itamar Procaccia. "Dimensions and Entropies Of Strange Attractors From A Fluctuating Dynamics Approach," *Physica*, *8D*:435–444 (March 1983).
11. Jones, Alan L. *Image Segmentation Via Fractal Dimension*. MS thesis, School of Engineering, Air Force Institute of Technology (AU), Wright Patterson AFB, OH, December 1987.
12. Kostelich, Eric J. and Harry L. Swinney. *Practical Considerations in Estimating Dimension From Time Series Data*. Technical Report, University of Texas, October 1989.
13. Mandelbrot, Benoit B. *The Fractal Geometry of Nature*. New York: W.H. Freeman and Company, 1977.
14. Maneely, Mark Allen. *Fractal Geometry Segmentation of Polarimetric Synthetic Aperature Radar Images*. MS thesis, School of Engineering, Air Force Institute of Technology (AU), Wright Patterson AFB, OH, September 1989.

15. Moody, John and Christian Darken. "Learning with Localized Receptive Fields." In *Proceedings of the 1988 Connectionist Models Summer School*, pages 133–143, unknown 1988.

16. Morin, T. J. *Data Conversion Between ADT Image Formation Processor and the VAX Computer*. Technical Report 47PM-ADT-0053, Lexington, MA: Massachusetts Institute of Technology Lincoln Laboratory, November 1986.

17. Novak, L. M. and others. *Studies of Target Detection Algorithms That Use Polarimetric Radar Data*. Technical Report, Massachusetts Institute of Technology Lincoln Laboratory, October 1988.

18. Nowlan, Steven J. *Max Likelihood Competition in RBF Networks*. Technical Report CRG-TR-90-2, Toronto Canada: Department of Computer Science, University of Toronto, February 1990.

19. Peitgen, Heinz-Otto and Dietmar Saupe, editors. *The Science of Fractal Images*. New York: Springer-Verlag, 1988.

20. Pentland, Alex P. "Fractal-Based Description of Natural Scenes," *IEEE Transactions on Pattern Analysis and Machine Intelligence*, *PAMI-9*:661–674 (November 1984).

21. Recla, Wayne F. *A Study in Speech Recognition Using a Kohonen Neural Net, Dynamic Programming, and Multi–Feature Fusion*. MS thesis, School of Engineering, Air Force Institute of Technology (AU), Wright Patterson AFB, OH, December 1989.

22. Rogers, Steve, July 1990. Class Notes, EENG 817, Air Force Institue of Technology.

23. Simm, C. W. and others. "On the Analysis of Experimental Signals For Evidence of Deterministic Chaos," *Helvetica Physica Acta*, *60*:510–551 (August 1987).

24. Smith, Leonard A. "Intrinsic Limits On Dimension Calculations," *Physics Letters*, *133, Number 6*:283–288 (September 1988).

25. Stowe, Francis Scott. *Speech Recognition Using Kohonen Neural Networks, Dynamic Programming, and Multi–Feature Fusion*. MS thesis, School of Engineering, Air Force Institute of Technology (AU), Wright Patterson AFB, OH, December 1990.

26. Theiler, James. *Spurious Dimension From Correlation Algorithms Applied to Limited Time–Series Data*. Technical Report, California Institute of Technology, May 1986.

27. Theiler, James. *Efficient Algorithm For Estimating The Correlation Dimension From A Set Of Discrete Points*. Technical Report, California Institute of Technology, March 1987.

28. Theiler, James. *Estimating Fractal Dimension*. Technical Report, Massachusetts Institute of Technology Lincoln Laboratory, April 1989.

29. Thomas, Scott G. *Angle of Arrival Detection through RBF Artificial Neural Network Analysis of Optical Fiber Intensity Patterns*. MS thesis, School of Engineering, Air Force Institute of Technology (AU), Wright-Patterson AFB OH, December 1990.

30. Voss, Richard F. "Fractals in Nature: Characterization, Measurement, and Simulation." In *SIGGRAPH '87*, 1987.

31. Zahirniak, Daniel R. *Characterization of Radar Signals Using Neural Networks*. MS thesis, School of Engineering, Air Force Institute of Technology (AU), Wright-Patterson AFB OH, December 1990.

Vita

Captain Joseph L. Brickey was born on 27 April 1959 in Rockwood, Tennessee. He graduated from Harriman High School in 1977 and enlisted in the United States Air Force. After attending various technical and survival courses he was assigned to Hellenikon Air Base, Athens, Greece where he spent three and a half years as an airborne maintenance technician on RC-135 aircraft. Under Air Force sponsorship he then attended the University of Tennessee, Knoxville, from which he received the degree of Bachelor of Science (High Honors) in Electrical Engineering. While at University of Tennessee, his areas of concentration were Plasma Science and Optics, and Systems and Networks. After graduation in August 1985, he attended Officer Training School and received his commission in December of 1985. He was then assigned to Headquarters Strategic Air Command, Offutt Air Force Base, Nebraska where he worked as Sensor Test Program Manager, evaluating sensor technologies for strategic applications until May 1989. He entered the School of Engineering, Air Force Institute of Technology, Wright-Patterson Air Force Base, Ohio in May 1989.

Permanent address:

Route 8 Box 544
Harriman, Tennessee 37"48

December 1990 *Master's Thesis*

Fractal Geometry Segmentation of High Resolution Polarimetric Synthetic Aperture Radar Data

Joseph Lee Brickey, Capt, USAF

Air Force Institute of Technology, WPAFB OH 45433-6583

AFIT/GE/ENG/90D-06

WRDC/AARA, WPAFB OH 45433

Approved for Public Release; Distribution Unlimited.

This thesis investigated the potential of fractal dimension estimation for segmenting high resolution polarimetric synthetic aperture radar. The data used during this research were collected with the Advanced Detection Technology Sensor (ADTS) developed by Massachusetts Institute of Technology Lincoln Laboratory with Defense Advanced Research Projects Agency funding. ADTS is a fully polarimetric calibrated 35 GHz SAR with one foot impulse response. A method of applying the correlation dimension algorithm developed by Grassberger and Procaccia for estimating the dimension of time series data was implemented to estimate the correlation dimension of polarimetric SAR data.

A threshold sensitivity study was performed to determine which combination of polarizations used to calculate the correlation dimension resulted in the most accurately segmented image. Correlation dimension estimates were shown to be valid and robust features for segmenting ADTS imagery into culture, tree, field, and shadow regions. Simple thresholding and median filtering of correlation dimension estimates calculated from non–overlapping windows of ADTS imagery produced segmented imagery that was consistently over 90% accurate when using all four linear polarizations. An approach was implemented for automatically distinguishing between different classes of naturally occurring regions within the SAR image using correlation dimension estimates as input features to artificial neural networks.

Fractal Geometry, Fractal Dimension, Correlation Dimension, Synthetic Aperture Radar, Polarimetric, Segmentation, Kohonen Neural Network, Radial Basis Function

117

Unclassified Unclassified Unclassified UI